Cryo-EM structure of the polyphosphate polymerase VTC: Coupling polymer synthesis to membrane transit

Wei Liu[1#], Jiening Wang[2#], Véronique Comte-Miserez[3], Mengyu Zhang[1], Xuejing Yu[2], Qingfeng Chen[4], Henning Jacob Jessen[6], Andreas Mayer[3*], Shan Wu[2*], Sheng Ye[1,5*]

[1] Frontiers Science Center for Synthetic Biology (Ministry of Education), Tianjin Key Laboratory of Function and Application of Biological Macromolecular Structures, School of Life Sciences, Tianjin University, 92 Weijin Road, Nankai District, Tianjin 300072, P.R. China;

[2] State Key Laboratory of Biocatalysis and Enzyme Engineering, Hubei Collaborative Innovation Center for Green Transformation of Bio-Resources, Hubei Key Laboratory of Industrial Biotechnology, School of Life Sciences, Hubei University, Wuhan, Hubei 430062, China;

[3] Département d'Immunobiologie, Université de Lausanne, 1066 Epalinges, Switzerland

[4] School of Life Sciences, Yunnan University, Kunming 650091, China

[5] Life Sciences Institute, Zhejiang University, Hangzhou, 310058 Zhejiang, China

[6] Institute of Organic Chemistry University of Freiburg, Albertstrasse 21, 79104 Freiburg, Germany & CIBSS – Centre for Integrative Biological Signalling Studies, University of Freiburg

[#] These authors contribute equally to this work

[*]Correspondence to:

Sheng Ye, School of Life Sciences, Tianjin University, 92 Weijin Road, Nankai District, Tianjin 300072, China; E-Mail: sye@tju.edu.cn

Shan Wu, School of Life Sciences, Hubei University, 368 Youyi Avenue, Wuchang District, Wuhan, Hubei 430062, China; E-mail: wushan91@hubu.edu.cn

Andreas Mayer, Département de Biochimie, Université de Lausanne, Lausanne, Switzerland, Email: andreas.mayer@unil.ch

ABSTRACT

The eukaryotic polyphosphate (polyP) polymerase complex VTC synthesizes polyP from adenosine triphosphate (ATP) and translocates polyP across the vacuolar membrane to maintain intracellular phosphate (P_i) homeostasis. To discover how VTC solves this fundamental aspect, we determined a cryo-electron microscopy structure of a VTC complex (Vtc4/Vtc3/Vtc1) purified from *Saccharomyces cerevisiae* at 3.1 Å resolution. The structure reveals a heteropentameric architecture of one Vtc4, one Vtc3 and three Vtc1 subunits. The transmembrane region forms a polyP-selective channel, probably adopting a resting state conformation, in which a latch-like, horizonal helix of Vtc4 limits the entrance. The catalytic Vtc4 central domain is located on top of the pseudo-symmetric polyP channel, creating a strongly electropositive pathway for nascent polyP that can couple synthesis to translocation. The SPX domain of the catalytic subunit Vtc4 stimulates polyP synthesis by VTC. The non-catalytic Vtc3 regulates VTC through a phosphorylatable loop. Our findings, along with the functional data, allow us to propose a mechanism of polyP channel gating and VTC complex activation.

48 **INTRODUCTION**

49 Phosphate (P_i) homeostasis is a tightly regulated process in all organisms. Cells
50 face major changes in demand and supply of P_i, for example during the S-phase, when
51 DNA is duplicated. While cells must meet these P_i demands, at the same time, they
52 must safeguard themselves against an excessive cytoplasmic P_i concentration, which
53 might have detrimental bioenergetic effects (Austin an Mayer, 2017). How cells
54 maintain intracellular P_i homeostasis is a fundamental question and of growing
55 interest for medicine and agriculture. Dysfunction of P_i homeostasis leads to
56 neurodegeneration of renal Fanconi Syndrome in humans (Ansermet *et al*, 2017;
57 Legati *et al*, 2015), severe growth retardation and dwarfism in plants (Liu *et al*, 2015;
58 Puga *et al*, 2014), and lethality in microorganisms (Sethuraman *et al*, 2001).

59 To strike the delicate balance between the biosynthetic requirements for P_i and
60 the risks of excessive cytoplasmic P_i, unicellular organisms maintain important P_i
61 stores in membrane-bound, acidocalcisome-like organelles in the form of inorganic
62 polyphosphates, a polymer of up to a thousand P_i units linked through phosphoric
63 anhydride bonds (Docampo & Huang, 2016). PolyP influences numerous processes in
64 eukaryotes, ranging from activation of inflammatory responses, wound healing and
65 blood clotting (Gerasimaite & Mayer, 2016; Hassanian *et al*, 2015; Hoac *et al*, 2013;
66 Holmstrom *et al*, 2013; Mailer *et al*, 2019; Moreno-Sanchez *et al*, 2012; Schepler *et*
67 *al*, 2022; Smith & Morrissey, 2014) to regulation of bone calcification, cation
68 acquisition (Klompmaker *et al*, 2017), protein polyphosphorylation (Azevedo *et al*,
69 2015; Azevedo *et al*, 2018; Bentley-DeSousa *et al*, 2018; Bondy-Chorney *et al*,

70 2020), protein folding (Gray *et al*, 2014), osmoregulation (Lander *et al*, 2013;
71 Rohloff & Docampo, 2008) and virulence of a series of pathogens (Ikeh *et al*, 2017).
72 PolyP can also have a major impact on cytosolic P_i homeostasis. Dysregulation of its
73 synthesis can drive cells into P_i starvation or a state of P_i excess (Desfougeres *et al*,
74 2016). In case of sudden P_i starvation, polyP from acidocalcisome-like vacuoles can
75 guarantee sufficient P_i reserves to finish the next cell cycle and make an ordered
76 transition into a robust quiescent state. PolyP also buffers transient spikes in P_i
77 consumption, which can occur during S-phase (Bru *et al*, 2016b).
78 In prokaryotes, the polyphosphate kinase PPK1/2 catalyzes the transfer of the γ-
79 phosphate from ATP to produce polyP chains (Akiyama *et al*, 1992). Despite the
80 widespread presence of polyP and acidocalcisome-like vacuoles in eukaryotes, only a
81 single eukaryotic-type polyP-synthesizing enzyme could so far be isolated. This
82 vacuolar transporter chaperone (VTC) complex, originally identified in yeast but with
83 homologs in a wide variety of lower eukaryotes, has provided insights into the
84 mechanisms underlying the polyP synthesis (Hothorn *et al*, 2009). The aim of this
85 study is to address three fundamental questions related to the VTC complex. The first
86 question is related to the stoichiometry and the assembly of native VTC complexes.
87 VTC complexes of *Saccharomyces cerevisiae* contains at least four subunits: Vtc1,
88 Vtc2, Vtc3 and Vtc4 (Cohen *et al*, 1999; Muller *et al*, 2002), for which homologs can
89 readily be identified in other organisms. Vtc1 is a small membrane protein only
90 containing three transmembrane helices. Vtc2, Vtc3 and Vtc4 are highly homologous
91 in sequence, share a similar transmembrane domain with Vtc1 at the C-terminus, and

92 have an N-terminal SPX (Syg1/Pho81/XPR1) domain that plays key role in P_i
93 homeostasis (Wild *et al*, 2016), and a tunnel-shaped, central domain (Hothorn *et al.*,
94 2009). The central domain of Vtc4 is a polyP polymerase that synthesizes
95 polyphosphate using ATP as a substrate, while that of Vtc2 or Vtc3 is catalytically
96 inactive (Hothorn *et al.*, 2009; Wild *et al.*, 2016). A further subunit, Vtc5, can
97 associate with VTC. While its domain structure is similar to that of Vtc2, Vtc3 and
98 Vtc4, the Vtc5 sequence is highly diverged. Vtc5 can stimulate VTC but is not
99 essential for its activity, nor for its regulation by 5-IP_7, suggesting that it is an optional
100 regulatory subunit (Desfougères et al., 2016).
101 Crystal structures of the central domains of Vtc2 and Vtc4, and the SPX domain
102 of Vtc4 had been determined (Hothorn *et al.*, 2009). However, these structures leave
103 several questions open. They provide no information about the stoichiometry and the
104 assembly of VTC complexes. They also do not address a crucial functional aspect of
105 the VTC complex, that of a polyP translocase. To avoid the toxicity of the
106 accumulation of polyP in the cytoplasm, polyP synthesis and the immediate
107 translocation of polyP into the vacuole are coupled (Gerasimaite *et al*, 2014;
108 McCarthy *et al*, 2022). However, how they are coupled remains unclear. A third open
109 question is related to the regulation of VTC complexes. When cytosolic P_i
110 concentration is sufficiently high, VTC complexes should synthesize polyP, while
111 with low cytosolic P_i concentration, VTC complexes should be switched off to avoid
112 depletion of P_i from the cytosol (Desfougères et al., 2016). The activity of VTC
113 complexes is regulated through inositol-based signaling molecules, including the

114 highly phosphorylated, diffusible inositol polyphosphates (InsPs) and inositol
115 pyrophosphates (PP-InsPs) (Wild *et al.*, 2016; Gerasimaite et al., 2017).
116 To address these questions, we performed functional assays and cryo-EM
117 structural analysis on endogenous *Saccharomyces cerevisiae* VTC complex. The
118 cryo-EM structure, as well as the detailed functional assay, reveal an unexpected
119 heteropentameric architecture, a coupled polyP polymerase and translocase, a
120 stimulatory SPX domain, and a phosphorylation-dependent regulatory loop. It
121 provides insights into the activation and regulation mechanism of the VTC complex,
122 as well as the polyP channel gating mechanism.
123
124

125 **RESULTS**

126 **Purified VTC complex synthesizes polyP in an ATP- and inositol polyphosphate-**

127 **dependent manner**

128 The VTC complex of *Saccharomyces cerevisiae* contains four subunits: Vtc1,

129 Vtc2, Vtc3 and Vtc4 (Cohen *et al.*, 1999; Muller *et al.*, 2002). We first performed

130 pull-down assays and confirmed that no interaction exists between Vtc2 and Vtc3,

131 either directly or indirectly (Figure S1A), confirming the existence two different VTC

132 complexes, Vtc4/Vtc3/Vtc1 and Vtc4/Vtc2/Vtc1, as also revealed previously

133 (Hothorn *et al.*, 2009). Consistently, knockout of VTC1 or VTC4 alone, or of both

134 VTC2 and VTC3, significantly reduced the cellular PolyP content (Figure 1A),

135 indicating that the catalytic subunit Vtc4 is necessary but not sufficient for polyP

136 synthesis *in vivo*. Individual knockout of VTC2 or VTC3, which disrupted the

137 formation of only one of the two VTC complexes, did not significantly reduce cellular

138 polyP content (Figure 1A). Interestingly, knockout of VTC2 significantly enhanced

139 the cellular polyP content in the BJ2168 background that we used here (Figure 1A).

140 This indicates that Vtc4/Vtc3/Vtc1 and Vtc4/Vtc2/Vtc1 complexes independently

141 synthesize polyP and suggests a compensatory mechanism boosting the activity of

142 one complex when the other one loses function. This may maintain intracellular polyP

143 content.

144 We inserted an affinity tag (His-TEV-Protein A) at the C-terminus of either Vtc3

145 or Vtc2, and individually purified the endogenous Vtc4/Vtc3/Vtc1 and

146 Vtc4/Vtc2/Vtc1 complexes (Figure S1B, S1C). We performed the polyP synthesis

147 experiments on these intact VTC complexes and observed that both Vtc4/Vtc3/Vtc1
148 and Vtc4/Vtc2/Vtc1 complexes retain the ability to synthesize polyP from ATP *in*
149 *vitro* in a divalent cation dependent manner (Figure S2A, S2B), in agreement with a
150 previous study revealing that the central domain ($Vtc4^{189-480}$) of Vtc4 is a polyP
151 polymerase (Hothorn *et al.*, 2009). The synthesized polyP could be degraded by Ppx1,
152 a polyphosphatase in yeast that specifically hydrolyzes polyP (Figure S2A). While
153 ATP, GTP and CTP all interact with the central domain of Vtc4 with binding
154 affinities in the micromolar range (Hothorn *et al.*, 2009), polyP synthesis was
155 significantly reduced when ATP was replaced with GTP, an ATP analog sharing a
156 similar purine moiety, and it was completely eliminated upon the replacement of ATP
157 with CTP (Figure 1B, 1C). These data demonstrate that polyP synthesis by the VTC
158 complex is preferentially driven by ATP.
159 We next measured polyP synthesis as a function of ATP concentration (Figure
160 1D). VTC activity showed a steep, linear dependence on ATP concentration,
161 reaching saturation at 3-4 mM. With a K_m value of around 2 mM ATP, VTC shows a
162 low affinity for ATP, which could be relevant to regulate VTC activity in the cellular
163 context, as free cellular ATP levels in yeast have been estimated to be ~ 1–2 mM
164 (Ingram & Barnes, 2000; Ozalp *et al*, 2010; Pluskal *et al*, 2011). In a situation where
165 P_i is abundant and VTC is maximally activated through inositol pyrophosphates (PP-
166 InsPs), the high K_m value for ATP provides an inbuilt mechanism to downregulate
167 polyP synthesis if ATP supply of the cell runs low, avoiding depletion of the essential
168 ATP pool for building phosphate reserves. In this way, VTC could integrate cellular

169 energy status with the InsPP and SPX-dependent signaling of P_i availability through
170 the intracellular phosphate reception and signaling pathway (INPHORS; Austin,
171 2020).

172 In response to cellular P_i availability, PP-InsPs stimulate polyP synthesis. In line
173 with this, InsPs and PP-InsPs can activate VTC in vitro (Gerasimaite *et al*, 2017;
174 Lonetti *et al*, 2011; Wild *et al.*, 2016). While inositol pyrophosphates activate VTC
175 more strongly and at lower concentrations than $InsP_6$ (Gerasimaite et al., 2017), $InsP_6$
176 is commercially available and was used for many of our in vitro experiments for that
177 reason. We simplified the strain background because the two VTC complexes, are
178 enzymatically redundant. Analyzing the effect of substitutions would hence
179 necessitate to genetically manipulate both complexes in parallel. Furthermore, only
180 the Vtc3-containing complex resides entirely on vacuoles, whereas much of the
181 Vtc4/Vtc2/Vtc1 resides in the cell periphery (probably in the ER) (Uttenweiler et al.,
182 http://www.molbiolcell.org/cgi/doi/10.1091/mbc.E06 – 08 – 0664). To streamline the
183 approach, we focused the analysis on substitutions in the Vtc4/Vtc3/Vtc1 complex
184 and performed all further functional analyses in *VTC2* knockout cells to exclude
185 interference by the Vtc4/Vtc2/Vtc1 complex.

186 PolyP synthesis by purified VTC 4/3/1 complex was strongly stimulated by
187 $InsP_6$, especially at low concentrations of ATP (Figure 1D). Without the addition of
188 ATP, $InsP_6$ alone did not produce a fluorescence signal (Figure S2C). Given that the
189 VTC complex integrated in the intact membrane displays much higher activity than
190 the purified complex (Gerasimaite *et al.*, 2014), we also performed in vitro polyP

191 synthesis experiments using isolated vacuoles. As shown in Figure 1E, the VTC
192 complex from purified vacuoles synthesized polyP in an ATP-dependent manner, and
193 PP-InsPs enhanced polyP synthesis more than 10-fold.

194 **Overall architecture of yeast Vtc4/Vtc3/Vtc1 complex**

195 To understand the polyP synthesis and transport mechanism, we analyzed the
196 purified Vtc4/Vtc3/Vtc1 complex by single-particle cryo-electron microscopy (Cryo-
197 EM), yielding a structure at an overall resolution of 3.1 Å (Figure S3, S4). The cryo-
198 EM density map was of sufficient quality to allow modeling of almost the entire
199 complex, including the N-terminal SPX domains, the central domains, the C-terminal
200 transmembrane (TM) domains of Vtc4 and Vtc3, and the TM domains of Vtc1
201 (Figure S5).

202 The structure of the Vtc4/Vtc3/Vtc1 complex reveals an unexpected
203 heteropentameric architecture with a subunit stoichiometry of one Vtc4, one Vtc3 and
204 three Vtc1 subunits (Figure 2A). The transmembrane domains of Vtc1, Vtc3 and
205 Vtc4, which share approximately 15% amino acid sequence identity, adopt similar
206 backbone conformations (Figure 2B). Three transmembrane helices (TM1-TM3) from
207 each subunit assemble in a pseudo-symmetrical fashion forming a cylinder-shaped
208 pentameric transmembrane domain. When viewed from the cytoplasmic side, the
209 arrangement of subunits around the transmembrane domain is Vtc3-Vtc4-Vtc1-Vtc1-
210 Vtc1 in a counter-clockwise direction (Figure 2C). The arrangement results in a
211 different subunit packing environment for each Vtc1. We therefore refer to the three
212 Vtc1 subunits as Vtc1(α), Vtc1(β) and Vtc1(γ) for clarity (Figure 2C). The TM1

213 helices from each subunit form an inner ring lining a pore, which likely represents the
214 central pore for polyP translocation into the vacuole. The pore tapers as it traverses
215 towards the intravacuolar side of the membrane. The TM2 and TM3 helices from each
216 subunit form an outer ring surrounding the inner ring. Compared to Vtc1 or Vtc4, the
217 TM part of Vtc3 has an additional, amphipathic MX helix at the C-terminus (Figure
218 S6A). The MX helix of Vtc3 runs parallel to the vacuolar face of the membrane,
219 forming hydrophobic interactions with the TM2 and TM3 helices of Vtc4, and the
220 TM3 helix of Vtc3 (Figure S6B). Given that Vtc2 and Vtc3 share an MX helix with
221 high sequence identity (Figure S7), the MX helix of Vtc2 likely adopts the same
222 conformation and performs similar function in the Vtc4/Vtc2/Vtc1 and
223 Vtc4/Vtc3/Vtc1 complexes.
224 The structure of the Vtc4/Vtc3/Vtc1 complex reveals an asymmetrical
225 arrangement of the cytosolic region in contrast to the relatively symmetrical
226 arrangement of the transmembrane region. Vtc4, Vtc3 and Vtc2 all contain an N-
227 terminal SPX domain, a central domain, and a C-terminal transmembrane domain
228 (Hothorn *et al.*, 2009; Wild *et al.*, 2016). The central domain ($Vtc4^{189-480}$) of Vtc4 is a
229 polyP polymerase, while those of Vtc2 and Vtc3 are catalytically inactive, likely
230 playing an accessory function (Hothorn *et al.*, 2009). Correspondingly, the
231 catalytically active central domain of Vtc4 is the only cytosolic domain that interacts
232 with the transmembrane pore (Figure S5). The catalytically inactive central domain of
233 Vtc3 stacks on top of the central domain of Vtc4 in a head to tail manner, forming a
234 heterodimer (Figure 2D). Interestingly, the two SPX domains adopt different positions

235 relative to the respective central domains. The SPX domain of Vtc4 locates at one
236 side of the central domain of Vtc4, using its α1 and α3 helices to interact with the α1
237 and α6 helices and the β6 and β7 strands of the central domain of Vtc4 (Figure 2D).
238 By contrast, the SPX domain of Vtc3 locates at the other side of the central domain of
239 Vtc3, using a different set of α helices (α1, α4, α5, α6 and α7) to interact with three
240 α helices (α2, α8 and α9) and two β strands (β4 and β5) of the central domain of
241 Vtc3 (Figure 2D). The asymmetrical arrangement of the cytosolic region of the
242 Vtc4/Vtc3/Vtc1 places both SPX domains close to each other on the same side of the
243 complex (Figure 2D). The SPX domain of Vtc4 not only interacts with the central
244 domain of Vtc4, but also interacts with two α helices (α1 and α9) of the central
245 domain of Vtc3 (Figure 2D). By contrast, the SPX domain of Vtc3 only interacts with
246 the central domain of Vtc3 (Figure 2D).

247 **PolyP channel in a resting and fastened state**

248 The transmembrane domain of the Vtc4/Vtc3/Vtc1 complex resembles a cylinder
249 formed from five subunits in a pseudo-symmetrical arrangement about a central axis.
250 The pore is lined by five TM1 helices, forming 'rings' of positively charged residues.
251 The cytoplasmic vestibule of the VTC channel contains two positively charged rings,
252 with K24 of Vtc1, K698 of Vtc3, and K622 of Vtc4 forming one, and R31 of Vtc1,
253 R705 of Vtc3, and R629 of Vtc4 forming the other one, rendering the surface strongly
254 electropositive (Figure 3A, 3B). These positively charged rings may constitute a
255 polyP selectivity filter in the vestibule of the VTC channel, and probably serve to
256 attract polyP to the channel mouth. To test the role of these rings for polyP synthesis

257 and translocation, we created 6 charge-reversing point mutations. All these mutations
258 significantly reduced cellular polyP content (Figure S8A), in line with previous
259 observations (Gerasimaite et al., 2014).

260 The TM1 helices taper inwards from the cytosolic side to the intravacuolar side,
261 with a ring of hydrophobic residues, including M42 of Vtc1, L716 of Vtc3, and L640
262 of Vtc4, defining the narrowest point, just 4 Å in diameter (Figure 3C, 3D, 3E). Since
263 this point is too narrow to permit the passage of polyP (with a Pauling radius of 3 Å)
264 the structure likely represents a non-conducting resting state of the pore.

265 In addition, the cytosolic entrance of the PolyP channel is fastened by a latch-
266 like, horizonal helix (HH) (Figure 3F, 3G). This helix is part of a linker of over
267 hundred residues connecting the central domain and the transmembrane domain of
268 Vtc4 (Figure S7). Most of the residues are hydrophilic, without density in the cryo-
269 EM map, indicating that the linker is highly flexible. However, the N-terminal part of
270 the linker (^{508}DFDEDDEDDAALVAAMT^{524}), which is rich in acidic residues, forms
271 an α helix horizontally latching the entrance of the transmembrane channel (Figure
272 3G). The N-terminus of the helix nestles at the Vtc1(γ)-Vtc3 interface, with the acidic
273 residues forming multiple salt bridges with the positively charged residues at the
274 channel mouth (Figure 3G). The C-terminus of the helix forms multiple hydrophobic
275 interactions with Vtc1(α) and Vtc1(β) (Figure 3G). To probe the importance of this
276 horizonal helix, we deleted it (residues 508-524) from Vtc4 and observed an
277 approximately 20% higher cellular polyP content in the respective mutant (Figure
278 S8B).

279 **Coupled polyP synthesis and translocation**

280 The structure of the Vtc4/Vtc3/Vtc1 complex clearly supports the concept of a
281 coupled polyP polymerase and translocase. The structures of the two central domains
282 of the Vtc4/Vtc3/Vtc1 complex are highly similar, with a r.m.s. deviation of 1.8 Å for
283 276 Cα atoms. Both central domains contain a central tunnel formed by antiparallel β
284 strands, with the majority of the α helices flanking the tunnel wall. The α helix (α7)
285 at the C-terminus of the central domain of Vtc4 forms a "helical plug" at one end of
286 the tunnel, reducing the tunnel to a small size only allowing polyP to pass (Figure S9).
287 The central domain of Vtc3 contains two additional α helices (α8 and α9) at the C-
288 terminus (Figure S9). These additional α helices, together with the SPX domain of
289 Vtc3, completely block one end of the tunnel of the central domain of Vtc3, likely
290 rendering it inactive (Figure S9). The tunnel walls are lined by conserved basic
291 residues (Figure 4A). Confirming its role as the catalytically active subunit of a polyP
292 polymerase, the Vtc4 central domain shows an endogenous Mn^{2+}-bound triphosphate
293 in the tunnel center (Figure S10). The Mn^{2+} is chelated by carboxylate oxygens of
294 E426 and the triphosphate oxygens in a distorted square-based pyramidal
295 configuration (Figure 4A). The triphosphate is coordinated by six conserved basic
296 residues (K200, R264, R266, K281, R361, K458), a serine (S457) and a tyrosine
297 (Y359) (Figure 4A). These residues are critical for polyP synthesis, as alanine
298 mutations of K200, R264, R266, K281, R361, K458, S457, and the phenylalanine
299 mutation of Y359, all significantly reduce polyP content of respective mutant cells
300 (Figure 4B). Structure based sequence alignment revealed that among these residues,

301 the only difference is K458 of Vtc4, which is I522 in Vtc2, and L527 in Vtc3 (Figure
302 S11A, S11B, S11C, S11D). Substituting K458 of Vtc4 to either leucine or isoleucine
303 significantly reduced polyP content, underlining the critical role of K458 for polyP
304 synthesis (Figure 4B).

305 Although the central domain and the transmembrane domain of Vtc4 are
306 covalently connected, most of the linker in between is flexible without observable
307 density in the cryo-EM map. The central domain of Vtc4 interacts with the
308 transmembrane pore via contacts between the β4-β5 loop of Vtc4 and the TM2-TM3
309 loop of Vtc3, as well as contacts between the loop before TM1 of Vtc4 and the β4-β5
310 loop, α2, and the loop after β11 of Vtc4 (Figure 4C). The β4-β5 loop of Vtc4 is
311 extended and protrudes into a hydrophobic pocket formed between the
312 transmembrane domains of Vtc3 and Vtc4, with the aromatic side chain of Trp287
313 interacting with Val699, Leu774 and Leu765 of the TM2-TM3 loop of Vtc3, and
314 Pro621 of the loop before TM1 of Vtc4 (Figure 4C). To confirm the importance of the
315 observed interactions between the central domain of Vtc4 and the transmembrane
316 pore, we created point mutants designed to disrupt the hydrophobic contact by
317 changing hydrophobic residues to acidic residues and observed that they all
318 significantly reduce cellular polyP content (Figure 4D).

319 The interactions bring the catalytically active central domain of Vtc4 near the
320 transmembrane pore, with the tunnel walls directly connecting to the vestibule of the
321 pore. Superposition of the previously determined central domain of Vtc4 (Hothorn *et*
322 *al.*, 2009) with the one determined in this study reveals that the phosphate polymer

323 overlaps with the triphosphate and winds through the tunnel towards the vestibule of
324 the pore (Figure 4E), suggesting that the nascent polyP travels from the active site of
325 the central domain of Vtc4 to the vestibule of the transmembrane pore, thus
326 translocating across the membrane. In addition, the traveling pathway of polyP is
327 strongly electropositive, which probably feeds the polyP product through the
328 membrane pore into the lumen of the vacuole. To confirm the importance of the
329 electropositive pathway, we created point mutants designed to switch the electrostatic
330 potential by changing positively charged residues to acidic residues and observed that
331 the intracellular content of polyP was significantly reduced (Figure 4F).

332 **The SPX domain of Vtc4 is critical for polyP synthesis and PP-InsPs regulation**

333 Both Vtc3 and Vtc4 contain an N-terminal SPX domain that may relay
334 information about the cellular P_i levels. The structures of the two SPX domains are
335 highly similar, with a r.m.s. deviation of 1.7 Å for 135 Cα atoms. Both SPX domains
336 share an N-terminal helical hairpin formed by two small helices, αI and αII, and a
337 three-helix bundle formed by two long helices, αIII and αIV, together with two
338 smaller C-terminal helices, αV and αVI (Figure S7). The SPX domain of Vtc3
339 contains an additional helix, αVII, at the C-terminus (Figure 5A), forming
340 hydrophobic interactions with αIV and αVI helices (Figure 5A). Both SPX domains
341 harbor a positively charged surface formed by multiple conserved lysine residues
342 from helices αII and αIV (Figure S12B, S12C), and can interact with a phosphate-
343 containing ligand with little specificity and selectivity (Wild *et al.*, 2016).

344 An interesting aspect of the Vtc4/Vtc3/Vtc1 complex is that the SPX domain of
345 Vtc4 interacts with both the central domain of Vtc3 and Vtc4 while the SPX domain
346 of Vtc3 only interacts with the central domain of Vtc3. To probe the role of the two
347 SPX domains, we individually truncated the SPX domain of Vtc3 or Vtc4 and
348 performed polyP synthesis experiments on the purified mutant Vtc4/Vtc3/Vtc1
349 complexes (Figure S13A, S13B). Truncation of the SPX domain of Vtc3 reduced
350 polyP synthesis activity of the complex only slightly and preserved the stimulation of
351 its activity by $InsP_6$ (Figure S13C), indicating that the SPX domain of Vtc3 is not
352 essential for stimulation of polyP synthesis by $InsP_6$. By contrast, truncation of the
353 SPX domain of Vtc4 significantly impaired polyP synthesis activity of the
354 Vtc4/Vtc3/Vtc1 complex (Figure S13C) and addition of $InsP_6$ reduced this activity
355 further instead of stimulating it (Figure S13C). Thus, the SPX domain of Vtc4 is
356 critical for polyP synthesis and $InsP_6$ regulation. Isolated vacuoles carrying the
357 truncated Vtc4/Vtc3/Vtc1 complex lacking the SPX domain of Vtc4 completely lose
358 polyP synthesis activity. Furthermore, addition of 5-$InsP_7$ or 1,5-$InsP_8$ no longer
359 stimulates the polyP synthesis activity (Figure 5B). While vacuoles carrying a
360 truncation of the SPX domain of Vtc3 generate less polyP than wild type, addition of
361 5-$InsP_7$ or 1,5-$InsP_8$ enhances this polyP synthesis activity (Figure 5B). Taken
362 together, the data of purified complex and isolated vacuole all demonstrate that the
363 SPX domain of Vtc4 is critical for polyP synthesis and PP-InsPs regulation.
364 The structure of the Vtc4/Vtc3/Vtc1 complex reveals that the positively charged
365 surface of the SPX domain of Vtc4 is close to the α1 helix of Vtc3 (Figure 5C). Two

366 arginine residues of the α1 helix of Vtc3, R223 and R226, are strictly conserved
367 between Vtc2 and Vtc3 (Figure S7). To probe the potential role of these conserved
368 arginine residues in $InsP_6$ regulation, we substituted them with acidic residues and
369 performed the polyP synthesis experiments on the purified mutant Vtc4/Vtc3/Vtc1
370 complexes (Figure S14A, S14B). Compared with the wild type complex, both mutant
371 complexes display significantly reduced polyP synthesis in the absence of $InsP_6$, with
372 a 50% reduced activity for the R226E mutant (Figure S14C). However, addition of
373 $InsP_6$ strongly stimulated the mutant complexes, reducing the difference to the
374 wildtype complex to only 10-20% (Figure 5D). Isolated vacuoles carrying the mutant
375 Vtc4/Vtc3/Vtc1 complex showed similar results as the purified complexes: Addition
376 of 5-$InsP_7$ or 1,5-$InsP_8$ strongly enhanced the polyP synthesis activity, leaving little
377 difference between the substituted complexes and the wildtype (Figure 5D).
378
379 **A regulatory loop of VTC3**
380 An interesting aspect of the Vtc4/Vtc3/Vtc1 complex is the conformation and
381 orientation of a loop between α1 and β2 of the central domain of Vtc3. In comparison
382 with Vtc4, this loop of Vtc3 is unusually long, containing over sixty amino acids
383 (Figure S7). The N-terminal half of the loop (^{228}LPALVYASVPNENDDFVDNLES
384 D^{250}), which is rich in acidic residues, forms of a nine-residue loop
385 (^{228}LPALVYASV^{236}), a four-residue turn (^{237}PNEN^{240}), a five-residue loop
386 (^{241}DDFVD^{245}) and a five-residue turn (^{246}NLESD^{250}). It winds across the
387 heterodimeric interface between the two central domains and the tunnel exit of the

388 Vtc4 central domain, interacting with β1, α1, β2, β5, α4, α5 and β7 of Vtc4 (Figure
389 6A). The last five-residue turn loop (^{246}NLESD^{250}) of the loop is close to the
390 triphosphate observed in the structure and forms multiple interactions with positively
391 charged residues of Vtc4, including R196, R280, K281, K294, K300, R373 and K428,
392 suggesting a regulatory role on polyP synthesis of this loop (Figure 6A).

393 In an effort to probe the regulatory role of the loop, we first generated a truncated
394 form of Vtc3 by replacing this long loop (residues 234-292) with a short linker
395 (GGSGGS) and performed polyP synthesis experiments on the purified mutant
396 Vtc4/Vtc3/Vtc1 complex (Figure S15A, S15B). The mutant Vtc4/Vtc3/Vtc1 complex
397 retained a slightly higher polyP synthesis activity than the wildtype complex,
398 suggesting a potentially negative regulatory role of the loop (Figure 6B). Furthermore,
399 addition of $InsP_6$ enhanced polyP synthesis to similar degrees both for the mutant and
400 wildtype Vtc4/Vtc3/Vtc1 complexes, even at low concentrations of ATP (Figure 6C).
401 The modest effect of deleting the long loop led us to test the hypothesis that the loop
402 might have a potential negative regulatory function, which might be lost by its simple
403 truncation. We noticed that the C-terminal half of the loop
404 (^{251}VRVQPEARLNIG**S**K**S**N**S**L**SS** DGN**S**NQDVEIGK**S**KSVIFPQ**S**Y^{292}), without
405 visible EM density, contains a cluster of phosphorylation sites, suggesting possible
406 regulation by phosphorylation. To mimic a non-phosphorylated or a phosphorylated
407 state of the loop, we substituted six of its serine residues (S263, S265, S267, S269, S270,
408 S274) by either alanine or aspartate and performed the polyP synthesis experiments
409 with vacuoles purified from respective mutants. In the absence of PP-InsPs, vacuoles

410 carrying the alanine-substituted loop displayed more than 200% higher polyP synthesis
411 activity *in vitro* than vacuoles from wild type, whereas the phospho-mimetic aspartate
412 substituted form had a significantly reduced activity (Figure 6D). Addition of PP-InsPs
413 significantly enhanced polyP synthesis of both non-phosphorylated and
414 phosphomimetic forms, conveying similar activity as for the wildtype form (Figure 6D).
415 This is consistent with a negative regulatory role of the loop, silencing the complex
416 when P_i (and hence PP-InsPs) are low. This silencing role may be enhanced by its
417 phosphorylation. When P_i becomes abundant, silencing may be overridden by the
418 increase in PP-InsPs. The loop might thereby enhance the dynamic range over which
419 VTC can be regulated, supporting a complete shut-down of polyP synthesis under P_i
420 starvation while preserving the potential for full activation when P_i is abundant. Given
421 that Vtc2 and Vtc3 share a same loop with high sequence identity (Figure S7), the loop
422 of Vtc2 likely adopts the same conformation and orientation and performs similar
423 regulatory function as the loop in Vtc3.

424 **Mechanics of polyP channel gating**

425 How the TM1 helices move to open the polyP channel of the VTC complex is a
426 difficult question to answer without a structure for the open state. Nevertheless, the
427 polyP channel in its resting and fastened state provides valuable hints on
428 conformational changes that may gate the polyP channel. First, the five-fold
429 symmetry of the polyP channel is broken, as revealed by the two distorted pentagons
430 connecting the adjacent Cαs of the two positively charged rings at the cytoplasmic
431 vestibule of the VTC channel (Figure 7A). The inter-subunit interfaces are extensive.

432 We define principal (+) and complementary (-) subunits and interfaces (Figure 7B),
433 where the principal (+) interface is made up of TM1 and TM3 of the principal
434 subunit, while the complementary (-) interface is made up of TM1 and TM2 of the
435 complementary subunit (Figure 4B). We superimposed the principal subunit of all the
436 five inter-subunit interfaces of the polyP channel, Vtc1(α)-Vtc1(β), Vtc1(β)-Vtc1(γ),
437 Vtc1(γ)-Vtc3, Vtc3-Vtc4 and Vtc4-Vtc1(α), and observed that the two
438 transmembrane domains forming the interface can have various relative positions,
439 with Vtc1(β)-Vtc1(γ) and Vtc3-Vtc4 packing tightly, Vtc1(γ)-Vtc3 loosely, and
440 Vtc1(α)-Vtc1(β) and Vtc4-Vtc1(α) in between (Figure 7B). Correspondingly, the
441 Vtc3-Vtc4 interface buries the most (4150 $Å^2$) protein surface area from solvent,
442 followed by Vtc1(β)-Vtc1(γ) (2920 $Å^2$), Vtc4-Vtc1(α) (2870 $Å^2$) and Vtc1(α)-
443 Vtc1(β) (2660 $Å^2$) interfaces. The Vtc1(γ)-Vtc3 interface has the smallest buried
444 surface area (2350 $Å^2$). This agrees with the observed asymmetry of the VTC channel.
445 Several reasons can account for the altered relative positioning at the inter-subunit
446 interfaces: Forces imposed by the latch-like, horizonal helix of Vtc4, and the
447 constraint of interacting with the central domain of Vtc4. The important point is,
448 however, that the inter-subunit interface is clearly flexible.
449 We also observed an unusual salt bridge among the mainly hydrophobic
450 interactions, at the center of the inter-subunit interface. E30 and R83 of Vtc1 are
451 strictly conserved among Vtc1, Vtc2, Vtc3 and Vtc4 from different species (Figure
452 7C). R83 from the principal (+) Vtc1 subunit forms a salt bridge with E30 of the
453 complementary (-) Vtc1 subunit. The corresponding residues are E704 and R762 of

454 Vtc3, and E628 and R681 of Vtc4 (Figure 7D). Similar salt bridges exist between
455 Vtc3 and Vtc4, and Vtc4 and Vtc1(α). However, R83 of Vtc1(γ) and E704 of Vtc3
456 are separated by 8 Å, too far to form a salt bridge (Figure 7D). To confirm the
457 importance of the observed inter-subunit salt bridge, we created 12-point mutants in
458 the VTC complex and measured their cellular polyP content. All substitutions
459 designed to disrupt the inter-subunit salt bridge by charge reversal or charge removal
460 significantly reduced cellular polyP content (Figure 7E), indicating that the inter-
461 subunit salt bridges are necessary for VTC complex function. To our surprise,
462 substitution of E704 of Vtc3, which does not form an inter-subunit salt bridge in the
463 structure, also significantly reduced cellular polyP content (Figure 7E). We hence
464 speculate that E704 of Vtc3 might form such an inter-subunit salt bridge in another
465 functional state of VTC, for example during VTC channel opening and transit of a
466 polyP chain. Due to their role in VTC complex function we term these salt bridges
467 inter-subunit "ionic locks".
468 The flexible nature of the inter-subunit interface, together with the observation of
469 inter-subunit "ionic locks", suggests a plausible polyP channel gating mechanism. We
470 assume that the polyP channel was captured in a resting state with the entrance
471 fastened by a latch-like, horizonal helix of Vtc4. The asymmetrical nestling of this
472 horizonal helix at the entrance of the channel imposes forces asymmetrically,
473 resulting in different relative positioning at the inter-subunit interfaces. Three loosely
474 packing inter-subunit interfaces, together with two tightly packing ones, render the
475 TM1 helices tapering from the cytosolic side towards the intravacuolar side,

476 generating a narrow point that might serve as a gate. The inter-subunit "ionic locks"
477 may hold the subunits together. During opening of the polyP channel, the horizontal
478 helix latch is lifted, and the subunits are pulled together by the "ionic locks", possibly
479 resulting in the formation of all five "ionic locks" between subunits. In this state, the
480 TM1 helices might tilt inwards at the cytosolic side and outwards at the intravacuolar
481 side, thus opening the channel (Figure 7F).
482

483 **Discussion**

484 **The observed central domain of Vtc4 exists in a polyP polymerase "off" state**

485 Three lines of evidence lead us to believe that the observed central domain of
486 Vtc4 in our cryo-EM structure is in a polyP polymerase "off" state. First, polyP
487 synthesis and the immediate translocation of polyP into the vacuole are coupled
488 (Gerasimaite *et al.*, 2014), and our structure of the Vtc4/Vtc3/Vtc1 complex supports
489 such coupling. Given that the polyP channel in our structure is in a resting state, it is
490 then reasonable to assume that also the polymerase is in the "off" state. Second, no
491 polyP product was observed in the cryo-EM structure of the whole Vtc4/Vtc3/Vtc1
492 complex. This should in principle be possible because active Vtc4 central domain,
493 synthesizing polyP from ATP, could be crystallized with its product bound, providing
494 a putative polymerase "on" state (Hothorn *et al.*, 2009). Third, structural comparison
495 revealed that the β4-β5 loop of the central domain of Vtc4 adopts a different
496 conformation between the crystal structure of the polyP-containing central domain of
497 Vtc4 alone (Hothorn *et al.*, 2009) and the cryo-EM structure of the whole

498 Vtc4/Vtc3/Vtc1 complex (Figure S16). This suggests a structural transition between
499 the putative active and inactive states. In line with this interpretation, the β4-β5 loop
500 of the central domain of Vtc4 is very sensitive to mutagenesis. Substitutions in this
501 region abolished polyP synthesis in vitro (E290G, E290A, E290R) and in vivo
502 (R284A/E285A/D286A) (Figure S16B, S16C).

503 **The activation mechanism of the VTC complex**

504 The data presented here have allowed us to elucidate a possible activation
505 mechanism of the VTC complex. We suppose that the VTC complex exists in
506 equilibrium between an inactive and active state. ATP and inositol pyrophosphates
507 activate the VTC complex. The Vtc4/Vtc3/Vtc1 structure was captured in an inactive
508 state, with a resting state polyP channel and an "off" state polyP polymerase. How
509 might the VTC complex convert the free energy of ATP binding, or the binding of the
510 inositol-based signaling molecules to turn "on" the polyP polymerase, and open the
511 polyP channel? To address this question, we superimposed the structures of isolated
512 SPX domains (SPX^{CtGde1}-$InsP_6$ (PDB ID: 5IJJ), or the SPX^{CtVtc4}-$InsP_6$ (PDB ID:
513 5IJP)) (Wild *et al.*, 2016) to the SPX domain of Vtc4 of the intact VTC complex, and
514 observed that the $InsP_6$ bound on the SPX domain is close to Vtc3 (Figure S17). The
515 SPX domain harbors a large, positively charged surface able to interact with
516 phosphate-containing inositol ligands but showing little specificity and selectivity at
517 the level of binding (Wild *et al.*, 2016). One can imagine that a phosphate-containing
518 ligand, such as ATP, 5-$InsP_7$ or 1,5-$InsP_8$, binds in the cleft between the large,
519 positively charged surface of the SPX domain of Vtc4 and the α1 helix of the central

520 domain of Vtc3 and causes the domains to move relative to each other, thus inducing
521 a conformational change that turns "on" the polyP polymerase, followed by the
522 opening of the polyP channel. In addition, it is worth noting that the binding affinity
523 of phosphate-containing ligands to SPX domain, gradually increase from P_i,
524 pyrophosphate (PP_i), triphosphate (PPP_i), to $InsP_6$, with a 20-fold lower K_d value of
525 $InsP_6$ than that of PPP_i (Wild *et al.*, 2016). This allowed us to propose a simplified
526 model of the regulation of the VTC complex (Figure 7G). The VTC complex contains
527 a polyP polymerase, a polyP channel and a regulatory cleft, and exists in equilibrium
528 between inactive and active states. The high apparent K_m value of VTC for ATP
529 might be an additional mechanism to reduce VTC activity in situations where P_i is
530 abundant but the cells cannot generate sufficient ATP to drive the conversion of large
531 amounts of P_i into polyP. Then, the high K_m would provide an inbuilt mechanism to
532 reduce polyP synthesis, which is a strong consumer of ATP but dispensable for
533 survival under such conditions. PP-InsPs might serve as high affinity stimulatory
534 ligands when ATP and P_i are abundant. Also the synthesis of InsPPs itself is probably
535 impacted by the ATP concentration, because both the $InsP_6$ kinases and PPIP kinases,
536 which synthesize 5-$InsP_7$ and 1,5-$InsP_8$, have high K_m values for ATP (Nair *et al*,
537 2018; Voglmaier *et al*, 1996), which are close to the ATP concentrations in the
538 cytosol. Thus, the VTC complex may integrate information about the ATP and
539 phosphate status of the cell at two levels. Such control at multiple levels may be
540 justified by the fact that VTC is a powerful phosphate pump: Powerful enough to push
541 the cells into phosphate starvation when overactivated (Austin & Mayer, 2020;

542 Desfougeres *et al.*, 2016); and capable of accumulating hundreds of millimolar of P_i

543 units in the form of polyP (Urech et al., 1978; DOI: 10.1007/BF00417851), which

544 must consume even higher concentrations of ATP.

545

546

547 **Materials and Methods**

548 **Yeast strains and plasmids**

549 The protease-deficient *S. cerevisiae* BJ2168 (MATa: leu2-3, trp1-289, ura3-52,

550 prb1-1122, pep4-3, prc1-407, gal2) was used as a host strain. The modified TAP tag

551 (6His-TEV-Protein A, named TAPm tag) or the strep tag was inserted at the C-

552 terminus of Vtc2 or Vtc3 by a homologous recombination-based method (Funakoshi

553 & Hochstrasser, 2009). Based on the above methods, we constructed Vtc2-TAPm,

554 Vtc3-TAPm and Vtc3(ΔC24)-TAPm single-tag strains, as well as Vtc2-TAPm/Vtc3-

555 Strep and Vtc2-Strep/Vtc3-TAPm dual-tag strains.

556 Single subunit knockout strains Vtc1Δ, Vtc2Δ, Vtc3Δ and Vtc4Δ were prepared

557 using a plasmid pYM27-kanMX in the BJ2168 strain. The kanMX gene replaces the

558 VTC gene behind the promoter of the corresponding subunit. Double subunits

559 knockout strain Vtc2Δ and Vtc3Δ were prepared using a plasmid p426-URA3 in the

560 Vtc3Δ strain.

561 The genes of Vtc1, Vtc2, Vtc3 and Vtc4 were cloned into plasmid p426-URA3

562 for various site-directed mutagenesis. Vtc1 point mutants were expressed from p426-

563 URA3 plasmid integrated into the genome behind the Vtc1 promotor of a

564 VTC1::kanMX strain. Similarly, Vtc2, Vtc3 and Vtc4 point mutants were performed
565 in the same way.
566 *S. cerevisiae* Ppx1 was cloned into pET28a (kanamycin selection) vector and
567 transferred to BL21 (DE3) for expression.
568 **Purification of the endogenous wild type and mutant VTC complexes**
569 Yeast cells were cultured in YPD (2% peptone, 1% yeast extract, 2% glucose)
570 medium for 18 hours. The cells were collected by centrifugation at 4,000 rpm at 4 °C.
571 The collected cells were resuspended in lysis buffer containing 25 mM Hepes-NaOH
572 (pH 7.4), 150 mM NaCl, 1 mM EDTA, and supplemented with a protease inhibitor
573 cocktail (2 μg/ml DNase I, 1 μg/ml pepstatin, 1 μg/ml leupeptin and 1 μg/ml
574 aprotinin, and 1 mM PMSF) and then were lysed using a high-pressure homogenizer
575 at 1,000 bar for 5 cycles. After lysis, cell debris was pelleted by centrifugation at
576 8,000g for 10 min. The supernatant was subjected to centrifugation in a Ti45 rotor
577 (Beckman) at 40,000 rpm at 4 °C for 1 hour. The pelleted membranes were
578 resuspended with a Dounce homogenizer in buffer A containing 25 mM Hepes-NaOH
579 (pH 7.4), 150 mM NaCl, 1 mM EDTA, 1 mM $MgCl_2$, 1 mM $MnCl_2$, 1 mM PMSF,
580 2% n-Dodecyl-β-D-Maltopyranoside (DDM, Anatrace), and 0.2% cholesteryl
581 hemisuccinate (CHS, Sigma Aldrich). After incubation at 4 °C for 3 hours, the
582 mixture was centrifuged at 18,000 rpm for 30 minutes to remove insolubilized
583 membrane. The supernatant was incubated with 600 μl IgG resin for 3 h. The beads
584 were washed with 30 ml buffer B (25 mM Hepes-NaOH (pH 7.4), 150 mM NaCl, 1
585 mM $MgCl_2$, 1 mM $MnCl_2$, 0.1% digitonin), and the complex was eluted with buffer B

586 containing 0.15 mg/ml TEV protease. The complex was concentrated and further
587 purified by size-exclusion chromatography on a Superose 6 10/300 Increase column,
588 equilibrated with buffer B. Peak fractions were pooled and concentrated to 8 mg/ml
589 for cryo-EM analysis.

590 **Cryo-EM grid preparation and data collection**

591 For the cryo-EM grids preparation, 3μl purified Vtc4/Vtc3/Vtc1 complex at a
592 concentration of approximately 8 mg/ml was applied respectively to glow-discharged
593 holey carbon EM grids (CryoMatrix Amorphous alloy film R1.2/1.3, 300 mesh). The
594 grids were blotted for 3 seconds with a blot force of 0 and then plunged into liquid
595 ethane using a FEI Vitrobot Mark IV (Thermo Fisher Scientific) at 4 °C and 100%
596 humidity. The cryo-EM grids were subsequently transferred into a 300kV Titan Krios
597 microscope (Thermo Fisher Scientific) equipped with a Gatan K3 direct electron
598 detector and a BioQuantum energy filter operated at a slit width of 20 eV.
599 Micrographs were automatically collected by EPU in super-resolution mode with a
600 pixel size of 0.4255 Å. Each micrograph was comprised of 40 frames with a total
601 exposure time of 2.5 seconds and total dose of 54 electrons per $Å^2$. The defocus range
602 for each micrograph was set from -1.0 to -1.5 μm.

603 **Cryo-EM data processing**

604 The collected movie stacks were summed and corrected for beam-induced
605 motion using MotionCor2 (Zheng *et al*, 2017) with a binning factor of 2. Gctf (Zhang,
606 2016) was used for estimating contrast transfer function (CTF) parameters for each
607 micrograph. And the following processing steps including particle picking, 2D

608 classification, 3D classification, 3D auto-refine, CTF refinement and polishing were
609 all performed using RELION-3.1.1 (Zivanov *et al*, 2020). Local resolution map was
610 estimated using RELION. All 3D density maps were displayed using UCSF Chimera
611 (Pettersen *et al*, 2004).

612 For the Vtc4/Vtc3/Vtc1 complex, 3871 and 3493 micrographs were collected
613 separately. And a total of 1,641,408 and 1,764,870 particles were auto-picked and
614 subjected to 2D classification and 3D classification individually. After that, good
615 classes showed clear features were combined from two datasets including 1,542,410
616 particles and subjected to another round of 3D classification. And two best-resolved
617 classes were chosen and combined containing 1,042,873 particles for 3D refinement,
618 CTF refinement and polishing. The final refinement generated a map with a global
619 resolution of 3.06 Å. And signal subtract was used for a more detailed feature and
620 higher resolution map of Transmembrane region.

621 **Cryo-EM model building, refinement and validation**

622 The initial templates of Vtc1, Vtc3 and Vtc4 were generated using AlphaFold2
623 (Jumper *et al*, 2021). The transmembrane domain, similar catalytic domain and SPX
624 domain of Vtc3 and transmembrane domain, catalytic domain and SPX domain of
625 Vtc4 were cut out and separately rigid body fitted into cryo-EM density map using
626 Chimera (Pettersen *et al.*, 2004). Then three copies of Vtc1 were docked into the
627 remaining density map. The initial fitting of Vtc4/Vtc3/Vtc1 complex was confirmed
628 by high agreement of secondary structural features between the predicted 3D models
629 and the cryo-EM density map. Polyphosphate and POV coordinates and geometry

630 restraints were generated using a phenix.elbow (Adams *et al*, 2010) and fitted into
631 density map. All the models were manual adjusted and rebuild using Coot (Emsley &
632 Cowtan, 2004), followed by several round of real-space refinement in PHENIX
633 (Adams *et al.*, 2010) and manual adjustment in COOT (Emsley & Cowtan, 2004).
634 The final model statistics were validated and provided by MolProbity (Williams *et al*,
635 2018) and summarized in Table S1. Structural figures were prepared using Chimera
636 (Pettersen *et al.*, 2004).

637 **Purification of recombinant ScPpx1**

638 *E.coli* BL21(DE3) cells were grown in LB medium containing 50 μg/ml
639 Kanamycin at 37 °C. 0.4 mM IPTG was added when OD600 reached 0.6. The cells
640 were transferred to 16 °C and cultured for 18 hours before harvesting. Cell pellets
641 were resuspended in lysis buffer containing 50 mM Hepes-NaOH (pH 7.4), 300 mM
642 NaCl and disrupted by sonication. After lysis, cell debris was removed by
643 centrifugation at 18,000 rpm for 30 minutes. The supernatant was incubated with 2 ml
644 Ni-NTA resin for 30 minutes. The beads were washed with 30 ml lysis buffer plus
645 20 mM imidazole, followed by a second wash with 30 mL of lysis buffer plus 50 mM
646 imidazole. The protein was eluted with lysis buffer plus 250 mM imidazole. The
647 eluted protein was dialyzed against 50 mM Hepes-NaOH (pH 7.4), 150 mM NaCl to
648 remove imidazole. Dialyzed protein was concentrated using an Amicon Ultra
649 concentrator (30 kDa MWCO, Millipore) and aliquoted into 100 μl amounts and
650 stored at −80 °C.

651 **Detection of PolyP content *in vivo***

652 Yeast cells (including wild-type strains, knockout strains and mutant strains)
653 were grown overnight in YPD medium. The yeast cultures were first diluted to an
654 OD_{600} value of 1, and the yeast cells were then collected from 2 ml of each culture by
655 centrifugation at 4000 rpm for 5 minutes.
656 PolyP extraction and purification are based on an improved method (Bru *et al*,
657 2016a). The cell pellet was resuspended with 400 μl of AE buffer (50 mM sodium
658 acetate (pH 5.3), 10 mM EDTA) at 4 °C, transferred to a screw cap tube containing
659 300 μl phenol and 40 μl 10% SDS, mixed by inversion 4 times, vortexed 5 seconds to
660 homogenize, incubated at 65°C for 10 minutes and chilled for 2 minutes on ice. The
661 tube was further added 300 μl chloroform, mixed by inversion 4 times, vortexed 5
662 seconds to homogenize and centrifuged at room temperature for 2 minutes at 14,000
663 rpm. The top aqueous phase was transferred to a prepared 1.5 ml screw cap tube
664 containing 350 μl chloroform, mixed by inversion 4 times, vortexed 5 seconds to
665 homogenize, centrifuged at room temperature at 14,000 rpm for 2 minutes. The
666 aqueous phase was then transferred to a new 1.5 ml microcentrifuge tube, added 2 μl
667 of RNase A (10 mg/ml) and 2 μl of DNase I (10 mg/ml), incubated at 37 °C for 1
668 hour, transferred to a pre-cold 1.5 ml microcentrifuge tube containing 1 ml of absolute
669 ethanol and 40 μl of 3 M sodium acetate (pH 5.3), leaved at -20 °C for 3 hours to
670 precipitate polyP and centrifuged for 20 min at 14,000 rpm at 4 °C. The supernatant
671 was discarded. The precipitant was further washed with the addition of 500 μl of 70%
672 ethanol, followed by centrifugation at 14,000 rpm at 4 °C for 10 minutes, and with the
673 supernatant discarded. The tube was left open to dry the small translucent-white polyP

674 pellet at room temperature for 10 minutes or until the pellet is completely dry. Finally,
675 the polyP was resuspended in 50 μl of deionized water. The polyP sample can be
676 directly measured or stored at -20 °C.

677 The purified polyP samples were measured by Malachite Green Phosphate Assay
678 Kits (Sigma, POMG-25H). First, PolyP needs to be degraded into Pi by the
679 polyphosphatase Ppx1. A 50 μl reaction system containing 5 μl PolyP, 0.5 μg Ppx1
680 and reaction buffer (50 mM Hepes-NaOH, pH 7.4, 150 mM NaCl) was leaved at
681 37 °C for 1 hour. The Malachite Green Phosphate Assay Kit is based on
682 quantification of the green complex formed between Malachite Green, molybdate and
683 free orthophosphate. The rapid color formation from the reaction can be conveniently
684 measured on a spectrophotometer (600 - 660 nm). Standard phosphate was used for
685 assay calibration.

686 **PolyP synthesis by purified VTC complex *in the absence or presence of $InsP_6$***

687 PolyP synthesis was assayed in 15 μl samples consisting of reaction buffer (25
688 mM Hepes-NaOH (pH 7.4), 150 mM NaCl, 1 mM $MgCl_2$, 1 mM $MnCl_2$, 0.1%
689 digitonin), 5 mM ATP and 6 μg purified endogenous proteins (Vtc4/2/1 complex, and
690 Vtc4/3/1 complex). When indicated, and 10 mM $InsP_6$ had been added. The entire
691 reaction was maintained at 4 °C for 1 hour, and the reaction was terminated with the
692 addition of the stop buffer (25 mM Hepes-NaOH (pH 7.4), 150 mM NaCl, 0.1%
693 digitonin, 15 mM EDTA, 15 μM DAPI) until the total volume reached 200 μl. The
694 addition of EDTA chelated the metal ions and quenched the catalytic activity of the
695 VTC complex. DAPI can form a complex with synthetic polyP, allowing the

696 measurement of the production of polyP based on the characteristic fluorescence
697 emission of DAPI-polyP complex at 550 nm. A total of 200 μl of the sample was
698 transferred into a black 96-well plate and fluorescence was measured with a
699 SPECTRAmax GEMINI XS fluorescence plate reader (Molecular Devices) using
700 λex=415 nm, λem=550 nm at 27˚C (Gerasimaite *et al.*, 2014).

701 **PolyP detection by PAGE gel**

702 *In vivo* purified polyP or *in vitro* synthesized polyP was mixed with one volume
703 of 2x TBE-Urea sample buffer (50% urea, 2x TBE, 0.25% xylene cyanol, 0.25%
704 bromphenol blue). The sample was resolved electrophoretically using a 12%
705 polyacrylamide gel (29:1 acrylamide /bis-acrylamide) containing 7 M urea in TBE
706 buffer pH 8.3, at 250 V/h at 4°C for 2.5 hours. The dimensions of the gel were 200
707 mm height, 200 mm wide and 1.5 mm thick. The gel was stained by soaking it in the
708 staining solution (25% methanol, 5% glycerol, 2 μg/ml DAPI, 50 mM Tris pH 10.5)
709 for 30 min, and de-stained by soaking it in de-staining solution (25% methanol, 5%
710 glycerol, 50 mM Tris pH 10.5) for 1 h. Finally, the gel was exposed to 254 nm UV
711 light in Syngene G-BOX trans-illuminator to visualize the polyP.

712 **Western blot detection of the interaction between Vtc2 and Vtc3**

713 The Vtc2-TAPm/Vtc3-Strep and Vtc2-Strep/Vtc3-TAPm strains were collected,
714 followed by disruption, membrane solubilization with detergent, and centrifugation.
715 The supernatant was incubated with IgG beads for 2 hours, followed by washing, and
716 the protein was eluted by TEV protease. Add reducing SDS sample buffer to the

717 samples and incubate at 75 °C for 5 minutes. Vtc2 and Vtc3 were detected using anti-
718 His and anti-Strep antibodies.

719 **Chemical synthesis and analysis of PP-InsPs**

720 Chemical synthesis and analysis of 5-$InsP_7$ and 1,5-$InsP_8$ were performed as
721 described previously (Pavlovic et al., https://doi.org/10.1038/ncomms10622).

722 **Isolation of vacuoles**

723 Vacuoles were essentially prepared as described (D'Agostino and Mayer, 2018;
724 https://doi.org/10.1007/978-1-4939-8760-3_16). The cells were grown in 1 liter
725 of YPD medium at 30 °C overnight and harvested at an OD_{600} of 0.6–1.3. A total of
726 600 ml of culture was centrifuged (2 minutes, 3900 g). Cells were resuspended in 50
727 ml of 0.1 M Tris-HCl pH 8.9, 10 mM DTT, incubated at 30 °C for 7 minutes in a
728 water bath and collected by centrifugation. Cells were resuspended in 15 ml of
729 spheroplasting buffer (50 mM potassium phosphate pH 7.5, 600 mM sorbitol in YPD
730 with 0.2% glucose), 3000–4500 units of recombinant lyticase (prepared from E.coli as
731 described in Reese and Mayer, 2005; doi:10.1038/nature03722) were added and
732 cells were incubated for 26 min at 30 °C in a water bath. Spheroplasts were collected
733 by centrifugation (3 min, 3400 g, 4 °C) and gently resuspended in 15 ml of 15%
734 Ficoll 400 in PS buffer (10 mM PIPES/KOH pH 6.8, 200 mM sorbitol). Spheroplasts
735 were lysed by adding DEAE-dextran to a concentration of 7 mg/l and incubated (2
736 min, 0 °C, then 2 min, 30˚C). Samples were chilled, transferred into SW41 tubes and
737 overlaid with 2.5 ml of 8% Ficoll 400, 3.5 ml of 4% Ficoll 400, and 1.5 ml of 0%
738 Ficoll 400 (all in PS buffer). After centrifugation (150,000 g, 90 minutes, 4 °C),

739 vacuoles were harvested from the 0–4% interface. When isolating vacuoles from
740 proteolytically competent strains, 1 mM PMSF and 16 protease inhibitor cocktail (16
741 PIC – 100 mM pefabloc SC, 100 ng/ml leupeptin, 50 mM O-phenanthroline and 500
742 ng/ml pepstatin A) were included in all buffers, starting from the spheroplasting step.
743 Vacuole amounts were determined by protein content, using the Bradford assay with
744 fatty-acid-free BSA as standard.

745 **PolyP synthesis by isolated vacuoles**

746 PolyP synthesis was assayed in 100-µl samples consisting of reaction buffer (10
747 mM PIPES/KOH pH 6.8, 150 mM KCl, 0.5 mM $MnCl_2$, 200 mM sorbitol) and ATP-
748 regenerating system (ATP-RS – 1 mM ATP-$MgCl_2$, 40 mM creatine phosphate and
749 0.25 mg/ml creatine kinase). The reactions were started by adding 2 mg of purified
750 vacuoles, the samples were incubated at 27˚C, followed by addition of 200 µl of stop
751 solution (12 mM EDTA, 0.15% Triton X-100 and 15 mM DAPI) in dilution buffer
752 (10 mM PIPES/KOH pH 6.8, 150 mM KCl, 200 mM sorbitol). This threefold dilution
753 with EDTA-containing buffer did not only stop nucleotide hydrolysis but also resulted
754 in faster development of DAPI–polyP fluorescence. Given that DAPI is membrane
755 impermeable, dissolving the membranes with detergent was required in order to detect
756 the entire polyP pool. A total of 240 µl of the sample was transferred into a black 96-
757 well plate and fluorescence was measured with a SPECTRAmax GEMINI XS
758 fluorescence plate reader (Molecular Devices) using λex=415 nm, λem=550 nm
759 (cutoff=530 nm) at 27˚C. Fluorescence was read every 1–2 min until the signal was

760 stable. Experiments were repeated with at least three independent vacuole
761 preparations. Values are presented as the mean±s.d.
762

763 **ACKNOWLEDGMENTS**

764 This work was supported in part by Ministry of Science and Technology
765 (2020YFA0908500 to S.Y. and 2020YFA0908400 to S.W.); the National Natural
766 Science Foundation of China (31971127 to S.Y. and 31900930 to S.W); China
767 Postdoctoral Science Foundation (2020M672434 to S.W.); the Fundamental Research
768 Funds for the Central Universities (to S.Y.); the ERC (788442 to AM); the SNSF
769 (CRSII5_170925 to AM); and the DFG (CIBSS – EXC-2189 – Project ID 390939984
770 to HJJ).

771 **Author contributions**

772 W.L. prepared the protein samples for cryo-EM and performed functional assays with
773 the assistance from M.Z. and Q.C.. J.W., X.Y. and S.W. performed cryo-EM sample
774 preparation, acquired cryo-EM data, data processing and analysis. H.Y and L.M
775 helped with cryo-EM data collection. V.C. and A.M. performed polyP synthesis
776 assays by isolated vacuoles. A.M. provided important insights and helped with
777 manuscript preparation. H.J.J. synthesized inositol pyrophosphates. S.Y. and W.L.
778 initiated the project, planned and analyzed experiments, supervised the research, and
779 wrote the manuscript with input from all co-authors.

780 **Competing interests**

781 The authors declare no competing financial interests.

782 **Data Availability**

783 The Structure coordinates and cryo-EM density maps have been deposited in the

784 protein data bank under accession number XXXX and EMD-XXXXX.

785

786

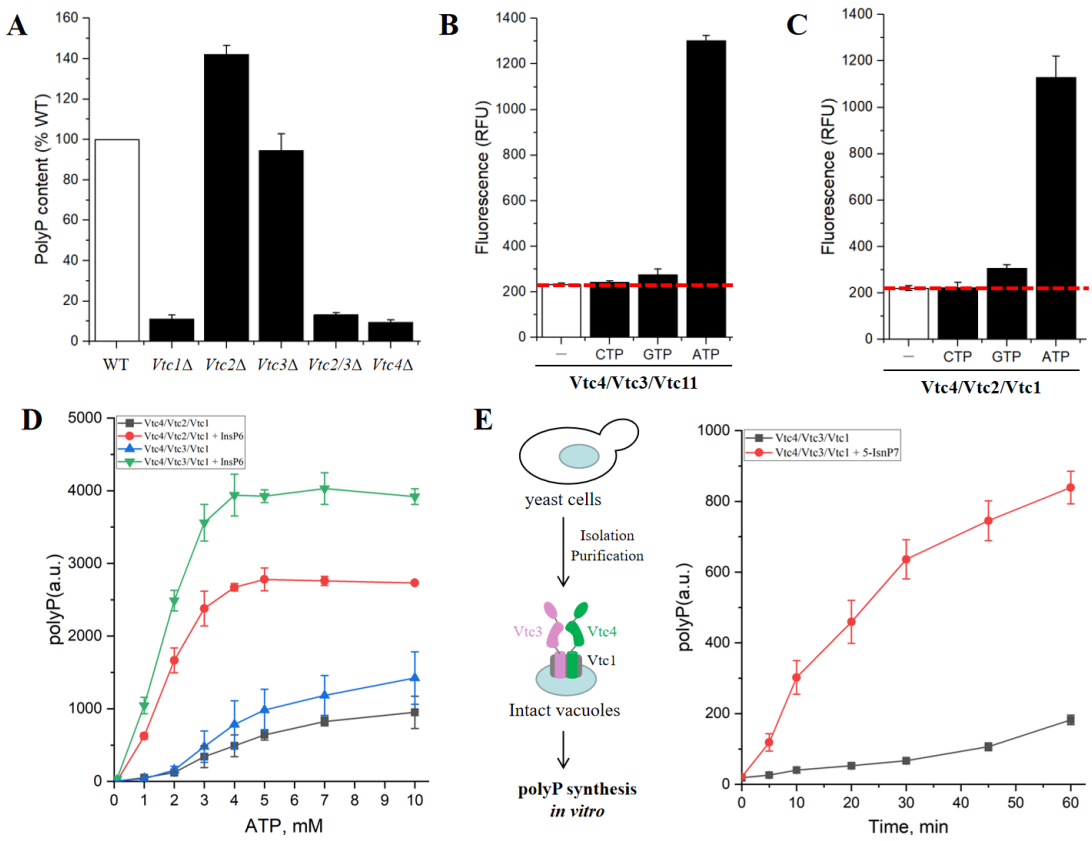

Figure 1. Functional characterization of VTC complexes

(A) PolyP accumulation *in vivo*. The polyP content of wild-type cells was set to 100%. Knockout of Vtc1, Vtc2, Vtc3 or Vtc4 impacts cellular polyP levels. Data show the mean±s.d (n=3).

(B and C) Purified endogenous (B) Vtc4/Vtc3/Vtc1 and (C) Vtc4/Vtc2/Vtc1 complexes synthesize polyP from ATP, GTP or CTP *in vitro*. 6 μg of Vtc4/3/1 complex or Vtc4/2/1 complex and 5 mM ATP/GTP/CTP were incubated for 60 min at 4°C, the reaction was stopped by the addition of 15 mM EDTA and 15 μM DAPI, and fluorescence was measured. Data show the mean±s.d (n=3).

(D) PolyP synthesis curves of purified endogenous Vtc4/3/1 and Vtc4/2/1 complexes at different ATP concentrations in the absence or presence of $InsP_6$ *in vitro*. The reaction system is detailed in Methods. Data show the mean±s.d (n=3).

(E) PolyP synthesis by isolated vacuoles carrying VTC complexes in the absence or presence of 1μM 5-$InsP_7$ *in vitro*. The reaction system is detailed in Methods. Data show the mean±s.d (n=3).

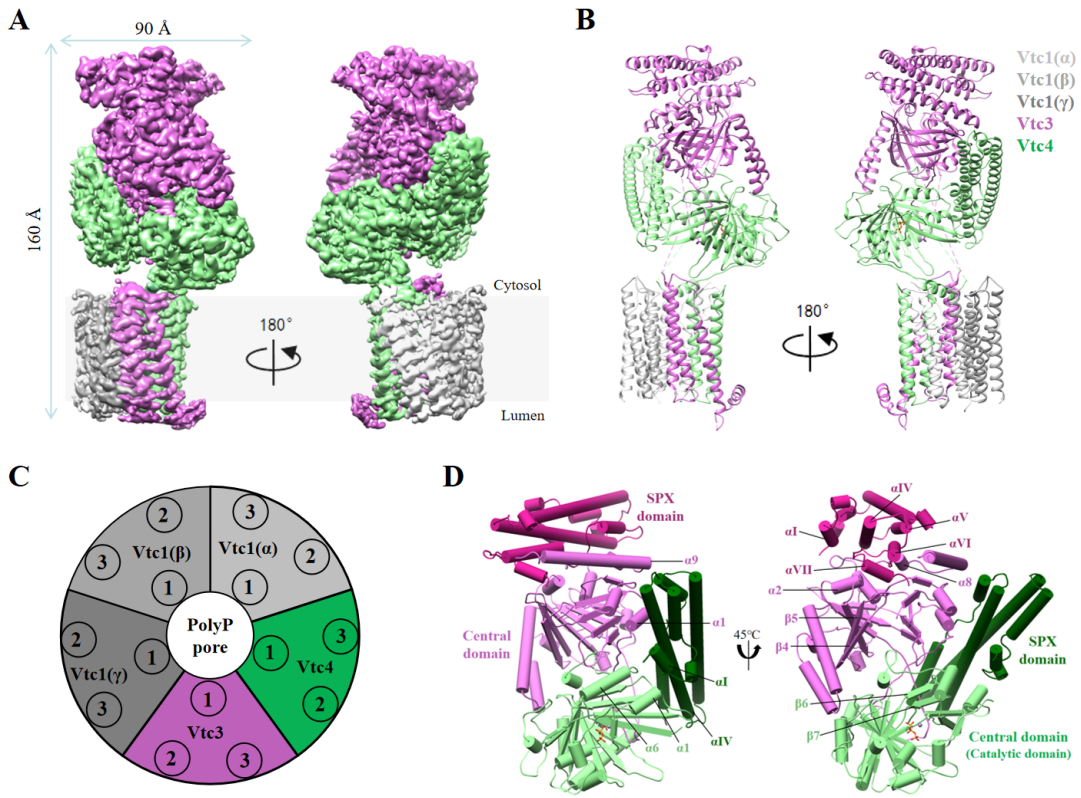

Figure 2. Structure of the yeast Vtc4/Vtc3/Vtc1 complex.

(A) Cryo-EM 3D map of the Vtc4/Vtc3/Vtc1 complex, showing front and back views. Color codes for the subunits of the complex are indicated.

(B) An atomic model shown in cartoon and colored as in A. The triphosphate and Mn^{2+} are shown in orange and brown, respectively.

(C) Top view of the model of Vtc4/Vtc3/Vtc1 complex. The numbers 1, 2 and 3 represent TM1, TM2 and TM3, respectively, where TM1 is at the N-terminus of the sequence and TM3 is at the C-terminus of the sequence.

(D) Structure of the asymmetrical arrangement of the intracellular region of the Vtc4/Vtc3/Vtc1 complex. The SPX domain and central domain of Vtc3 are shown in violet red and orchid, respectively; the SPX domain and central domain of Vtc4 are shown in dark green and light green, respectively.

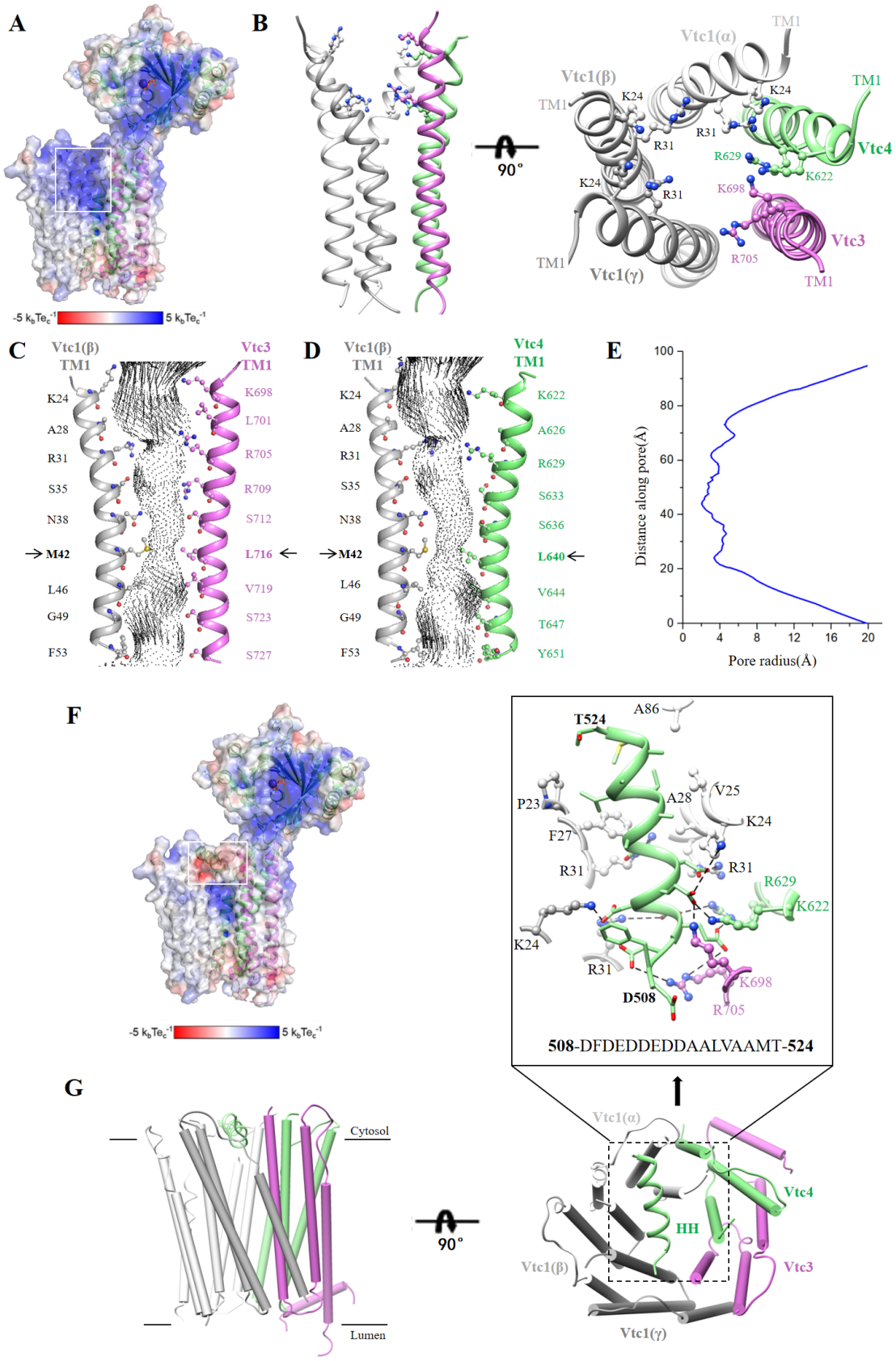

Figure 3. Conductance and permeation pore structure of the Vtc4/Vtc3/Vtc1 complex.

(A) Cutaway of the Vtc4/3/1 complex showing the electrostatic surface potential along the polyP-conducting pathway, excluding the horizontal helix, HH. The transparency of the electrostatic surface potential is set to 0.5.
(B) Side and top views of the structure of TM1 of Vtc4/Vtc3/Vtc1 complex. The cytoplasmic vestibule of the VTC channel contains two positively charged rings, with K24 of Vtc1, K698 of Vtc3, and K622 of Vtc4 forming one, and R31 of Vtc1, R705 of Vtc3, and R629 of Vtc4 forming the other one.
(C) TM1 α-helices from opposing Vtc1(β) and Vtc3 subunits with side chains shown for pore-lining residues. Spheres represent the solvent-accessible volume of the polyP channel. The black arrow points to the narrowest point of the channel.
(D) TM1 α-helices from opposing Vtc1(β) and Vtc4 subunits with side chains shown for pore-lining residues. Spheres represent the solvent-accessible volume of the polyP channel. The black arrow points to the narrowest point of the channel.
(E)Profile of the pore radius of the Vtc4/Vtc3/Vtc1 complex.
(F)Cutaway of the Vtc4/Vtc3/Vtc1 complex showing the electrostatic surface potential along the polyP-conducting pathway, including the horizontal helix, HH. The transparency of the electrostatic surface potential is set to 0.5.
(G) Side and top views of the structure of transmembrane helices of Vtc4/Vtc3/Vtc1 complex. Horizontal helix, HH (^{508}DFDEDDEDDAALVAAMT^{524}).

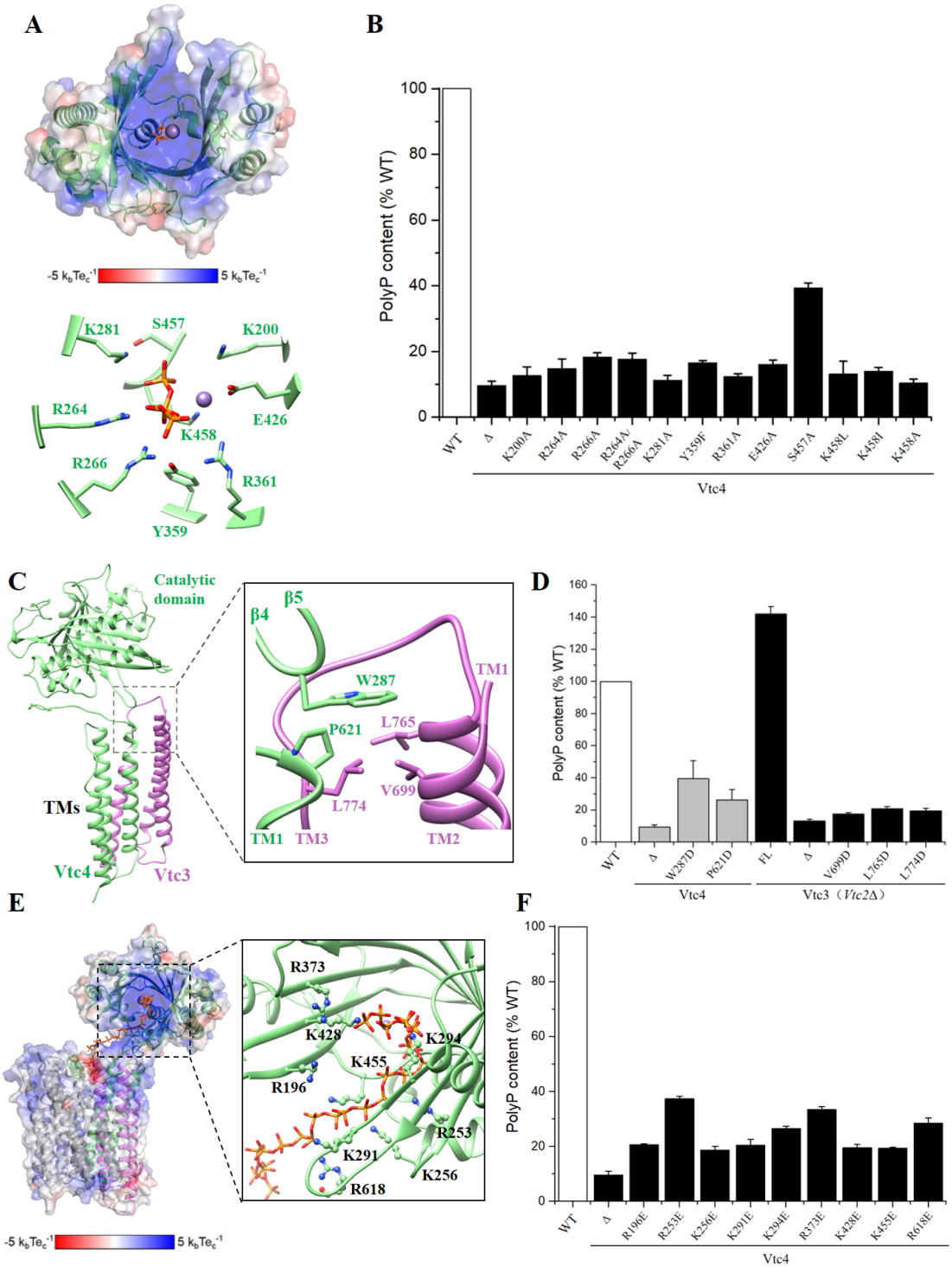

Figure 4. Structural and functional data of the VTC complex reveal that polyP synthesis and transport are coupled.

(A) Structure and electrostatic surface potential of the central domain of Vtc4. The triphosphate and Mn^{2+} are shown in orange and brown, respectively. Some key residues are shown.

(B) Cellular polyP content of Vtc4p point mutants expressed under the control of their native promoters in the *vtc4Δ* background. Data show the mean±s.d (n=3).

(C) Interactions between the β4-β5 loop of Vtc4 and the transmembrane domains of Vtc3 and Vtc4.
(D) Cellular polyP content of *VTC4* and *VTC3* point mutants expressed under the control of their native promoters in the *vtc4Δ* and *vtc3Δ*(*vtc2Δ*) backgrounds, respectively. Data show the mean±s.d (n=3).
(E) Superposition of the central domain of Vtc4 and the central domain of the polyP-bound Vtc4 (PDB: 3G3Q) structures. The structure of the central domain of polyP-bound Vtc4 is shown in blue. The polyP chains are shown in orange to overlap the triphosphates.
(F) Cellular polyP content of *VTC4* point mutants expressed under the control of their native promoters in the *vtc4Δ* backgrounds. Data show the mean±s.d (n=3).

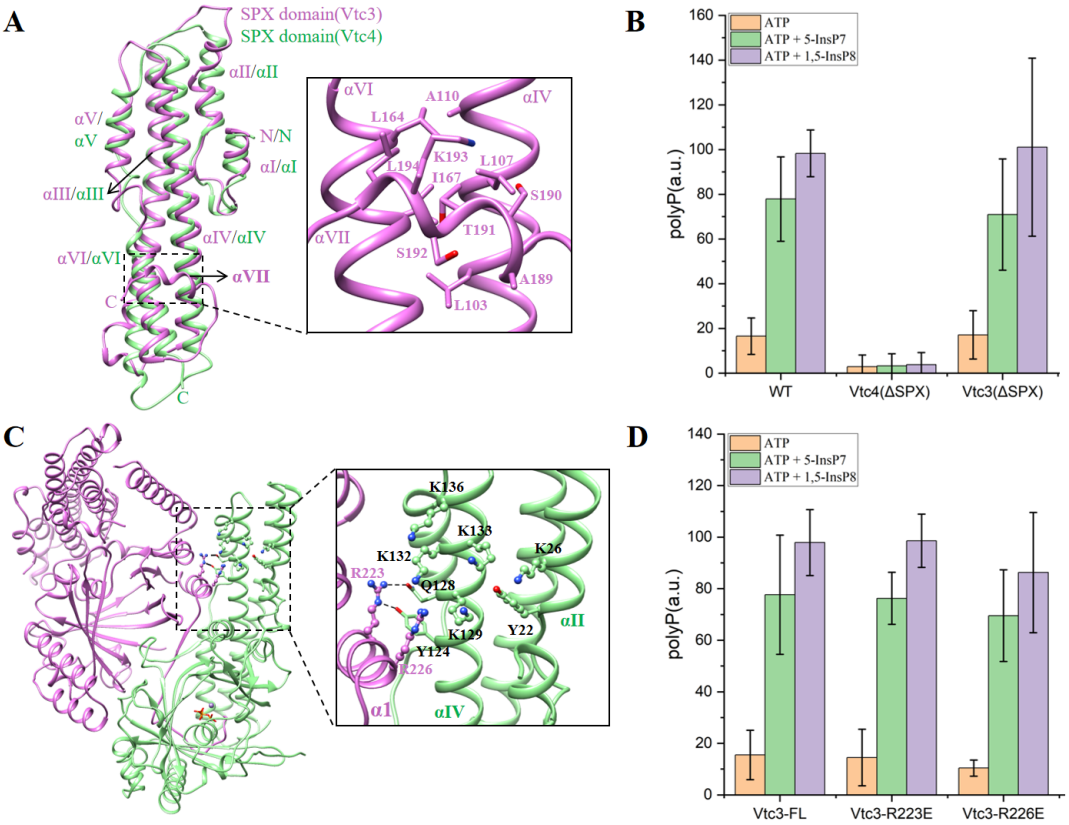

Figure 5. The SPX domain of Vtc4 regulates polyP synthesis in an PP-InsPs-dependent manner.

(A) Superposition of the SPX domain of Vtc4 and the SPX domain of Vtc3. The SPX domain of Vtc3 is shown in orchid, and the SPX domain of Vtc4 is shown in light green.

(B) PolyP synthesis by isolated vacuoles carrying Vtc4(ΔSPX)/Vtc3/Vtc1 complex, Vtc4/Vtc3(ΔSPX)/Vtc1 complex or Vtc4/Vtc3/Vtc1 complex in the absence or presence of 1 μM 5-$InsP_7$ or 1,5-$InsP_8$ *in vitro*. The reaction system is detailed in Methods. Data show the mean±s.d (n=3).

(C) Two conserved arginine residues on Vtc3 potentially involved in regulation by PP-InsPs.

(D) PolyP synthesis by isolated vacuoles carrying Vtc4/Vtc3(R223E)/Vtc1 complex, Vtc4/Vtc3(R226E)/Vtc1 complex or Vtc4/Vtc3/Vtc1 complex in the absence or presence of 1 μM 5-$InsP_7$ or 1,5-$InsP_8$ *in vitro*. The reaction system is detailed in Methods. Data show the mean±s.d (n=3).

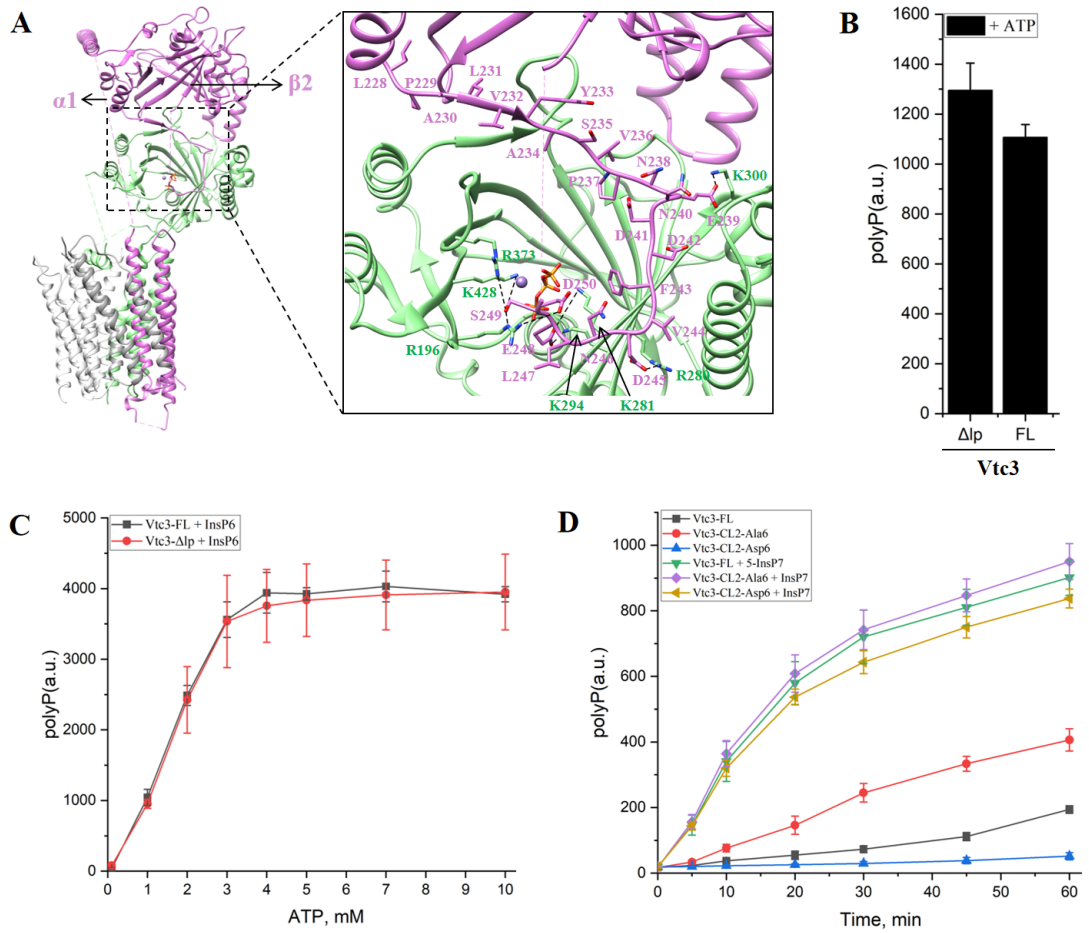

Figure 6. Structure and function of the regulatory loop of Vtc3.

(A) Structure of the regulatory loop of Vtc3. The loop is located between α1 and β2 of Vtc3, and the loop sequence consists of ^{228}LPALVYASVPNENDDFVDNLESD^{250}. Interactions (dotted lines) are shown.

(B) Purified truncated Vtc4/Vtc3(Δlp)/Vtc1 complexes synthesize polyP in the presence of ATP *in vitro*. Δlp indicates that the regulatory loop of Vtc3 (residues 234-292) was replaced by a small linker (GGSGGS). The reaction system is detailed in Methods. Data show the mean±s.d (n=3).

(C) PolyP synthesis curves of purified endogenous Vtc4/Vtc3/Vtc1 and truncated Vtc4/Vtc3(Δlp)/Vtc1 complexes at different ATP concentrations in the absence or presence of $InsP_6$ *in vitro*. The reaction system is detailed in Methods. Data show the mean±s.d (n=3).

(D) PolyP synthesis by isolated vacuoles carrying Vtc4/Vtc3(CL2-Ala6)/Vtc1 complex, Vtc4/Vtc3(CL2-Asp6)/Vtc1 complex or Vtc4/Vtc3/Vtc1 complex in the absence or presence of 1 μM 5-$InsP_7$ or 1,5-$InsP_8$ *in vitro*. The reaction system is detailed in Methods. Data show the mean±s.d (n=3).

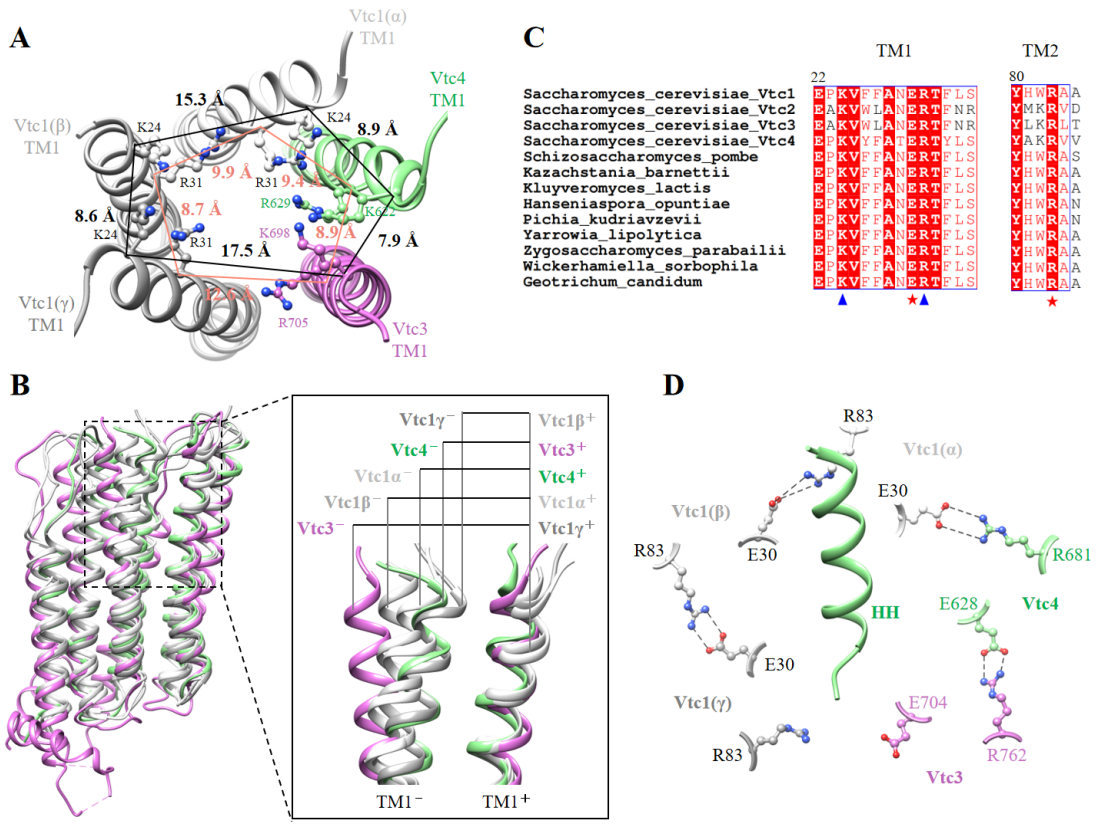
A
Vtc1(α) TM1
Vtc4 TM1
Vtc1(β) TM1
Vtc1(γ) TM1
Vtc3 TM1
15.3 Å
8.9 Å
9.9 Å
9.4 Å
8.7 Å
8.6 Å
8.9 Å
17.5 Å
7.9 Å
12.5 Å
K24
R31
R629
K622
K698
R705
B
Vtc1γ⁻
Vtc4⁻
Vtc1α⁻
Vtc1β⁻
Vtc3⁻
Vtc1β⁺
Vtc3⁺
Vtc4⁺
Vtc1α⁺
Vtc1γ⁺
TM1⁻
TM1⁺
C
TM1
TM2
22
80
Saccharomyces_cerevisiae_Vtc1
Saccharomyces_cerevisiae_Vtc2
Saccharomyces_cerevisiae_Vtc3
Saccharomyces_cerevisiae_Vtc4
Schizosaccharomyces_pombe
Kazachstania_barnettii
Kluyveromyces_lactis
Hanseniaspora_opuntiae
Pichia_kudriavzevii
Yarrowia_lipolytica
Zygosaccharomyces_parabailii
Wickerhamiella_sorbophila
Geotrichum_candidum
D
R83
Vtc1(α)
E30
Vtc1(β)
R681
HH
E628
Vtc4
Vtc1(γ)
E704
R762
Vtc3

897

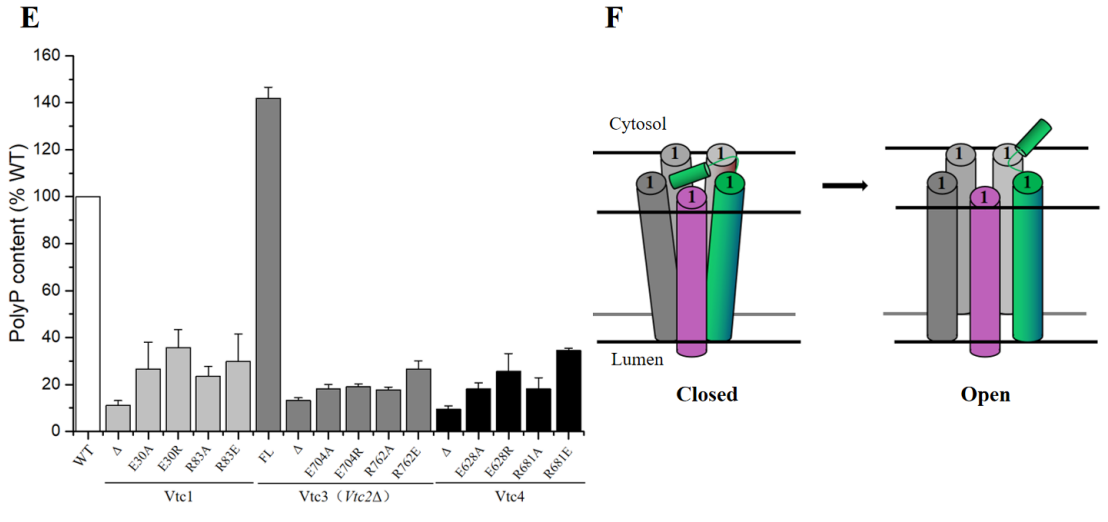
E
PolyP content (% WT)
160
140
120
100
80
60
40
20
0
WT
Δ
E30A
E30R
R83A
R83E
FL
Δ
E704A
E704R
R762A
R762E
Δ
E628A
E628R
R681A
R681E
Vtc1
Vtc3（Vtc2Δ）
Vtc4
F
Cytosol
Lumen
Closed
Open

898

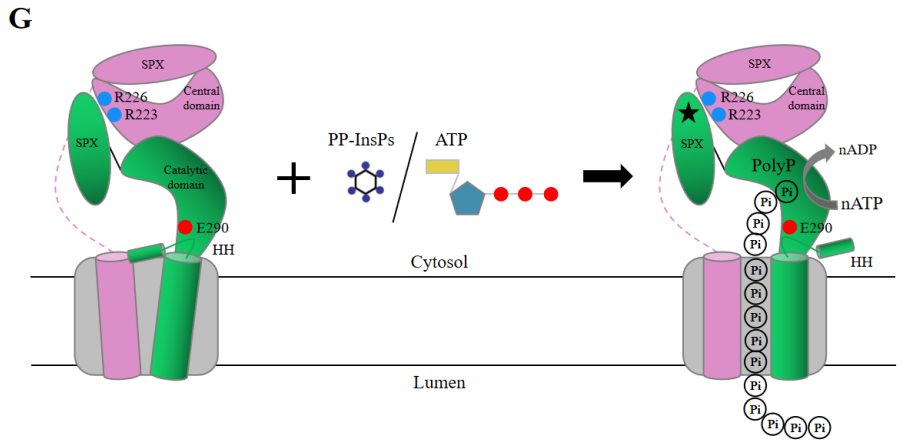
G
SPX
R226
R223
Central domain
SPX
Catalytic domain
E290
HH
PP-InsPs
ATP
Cytosol
Lumen
SPX
R226
R223
Central domain
SPX
PolyP
nADP
nATP
E290
HH
Pi

899

Figure 7. Asymmetric polyP channel and inter-subunit ionic locks

(A) Asymmetry in the channel at the level of the activation and desensitization gates. Residues at the polyP selectivity filter are shown in ball-and-stick representation. Distance between Cα of polyP selectivity filter residues are given in Å.

(B) Superposition of the principal subunits of all the five inter-subunit interfaces of the polyP channel.

(C) Sequence alignment of Vtc1, Vtc2, Vtc3 and Vtc4 from different species. Protein sequence numbers in NCBI: *Saccharomyces_cerevisiae*_Vtc1 (ID: NP_010995.1); *Saccharomyces_cerevisiae*_Vtc2 (ID: KZV11596.1); *Saccharomyces_cerevisiae*_Vtc3 (ID:KZV07497.1); *Saccharomyces_cerevisiae*_Vtc4 (ID:QHB096 08.1); *Schizosaccharomyces_pombe* (ID:NP_595683.1); *Kazachstania_barnettii* (ID:XP_041404278.1); *Kluyveromyces_lactis* (ID: QEU59996.1); *Hanseniaspora_opuntiae* (ID: OEJ89736.1); *Pichia_kudriavzevii* (ID:ONH77772.1); *Yarrowia_lipolytica* (ID: QNP96953.1); *Zygosaccharomyces_parabailii* (ID:AQZ10220.1); *Wickerhamiella_sorbophila* (ID: XP_024663738.1); *Geotrichum_candidum* (ID: CDO55024.1). Triangles and stars indicate key conserved amino acids, respectively.

(D) Multiple pairs of conserved salt bridges are formed at the inter-subunit interface of the VTC complex. R83 of Vtc1(γ) and E704 of Vtc3 are separated by 8 Å, too far to form a salt bridge.

(E) Cellular polyP content of *VTC4*, *VTC3* and *VTC1* point mutants expressed under the control of their native promoters in the *vtc4*Δ, *vtc3*Δ(*vtc2*Δ) and *vtc1*Δ backgrounds, respectively. Δ indicates that the entire subunit was knocked out. FL indicates full length, indicating that the subunit has not been modified in any way. Data show the mean±s.d (n=3).

(F) A model of the putative polyP channel gating mechanism. The schematic drawing illustrates conformational changes of the polyP channel switching between closed and open states. The number 1 represents the TM1 of each subunit of the VTC complex.

(G) A model of the activation mechanism of the VTC complex. Schematic of the Vtc4/3/1 complex. Subunits are colored. The three subunits of Vtc1 are shown in grey. Key amino acids are highlighted. The stars represent the binding sites of PP-InsPs or ATP.

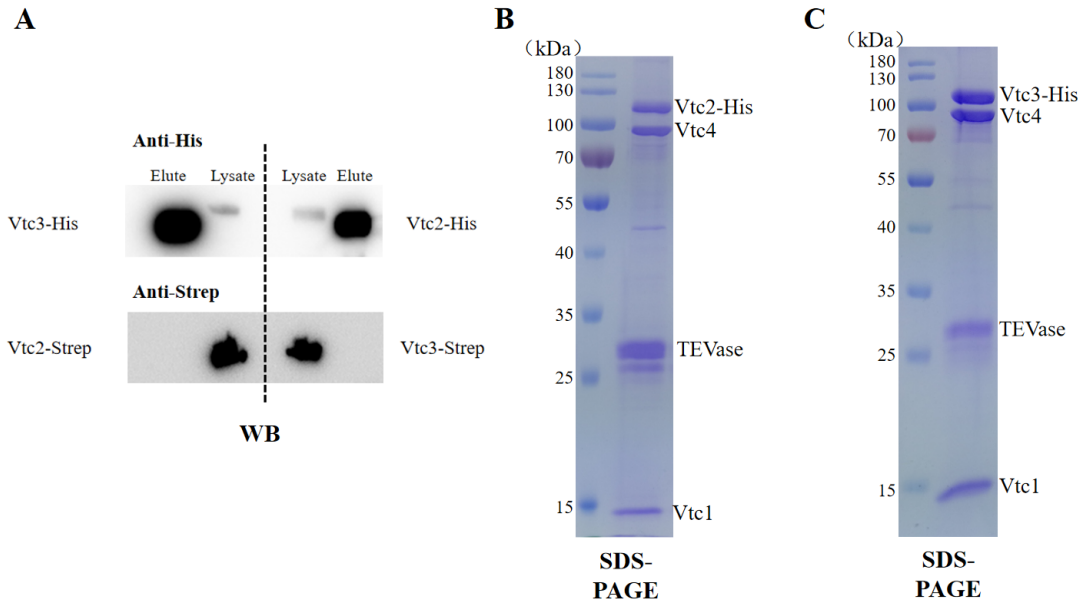

933

934 **Figure S1. Purification of endogenous VTC complexes from *Saccharomyces***
935 ***cerevisiae*.**
936 (A) The interaction between Vtc2 and Vtc3 was detected by co-immunoprecipitation.
937 The Vtc2-TAPm (-6His-TEV-Protein A)/Vtc3-Strep and Vtc2-Strep/Vtc3-TAPm
938 strains were constructed. Whole cell lysate was incubated with IgG resin for 2h,
939 followed by washing, and the protein was eluted by TEV protease. After the addition
940 of reducing SDS sample buffer and incubation at 75°C for 5 min, the protein samples
941 were run on SDS-PAGE gel. Vtc2 and Vtc3 were detected using anti-His_6 and anti-
942 Strep antibodies.
943 (B and C) Coomassie blue-stained SDS–PAGE gel of the purified (B) Vtc4/Vtc2/Vtc1
944 complex and (C) Vtc4/Vtc3/Vtc1 complex.
945

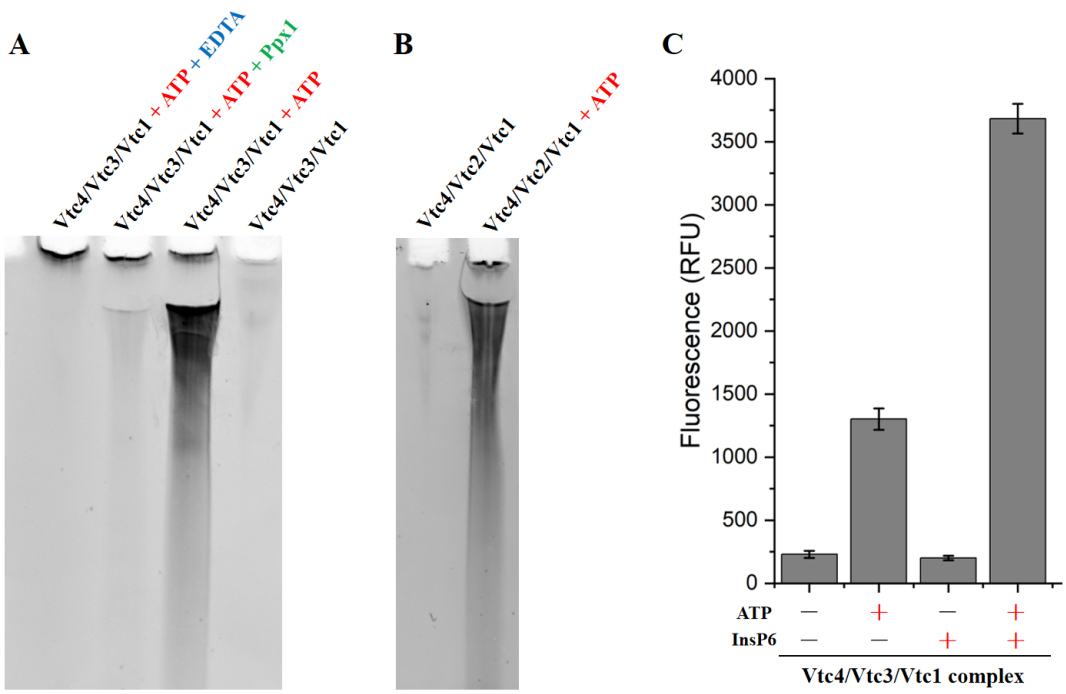

Figure S2. Purified endogenous VTC complexes synthesize polyP *in vitro*.
(A and B) Urea-PAGE of polyP synthesized by (A) Vtc4/Vtc3/Vtc1 complex and (B) Vtc4/Vtc2/Vtc1 complex *in vitro*. Synthetic polyP was fractionated in a 12% polyacrylamide gel, and polyP was visualized by negative DAPI staining. Ppx1: a polyphosphatase from yeast that specifically hydrolyzes polyP.
(C)The purified endogenous Vtc4/Vtc3/Vtc1 complex synthesizes polyP *in vitro* in an ATP- and $InsP_6$-dependent manner. Data show the mean±s.d.

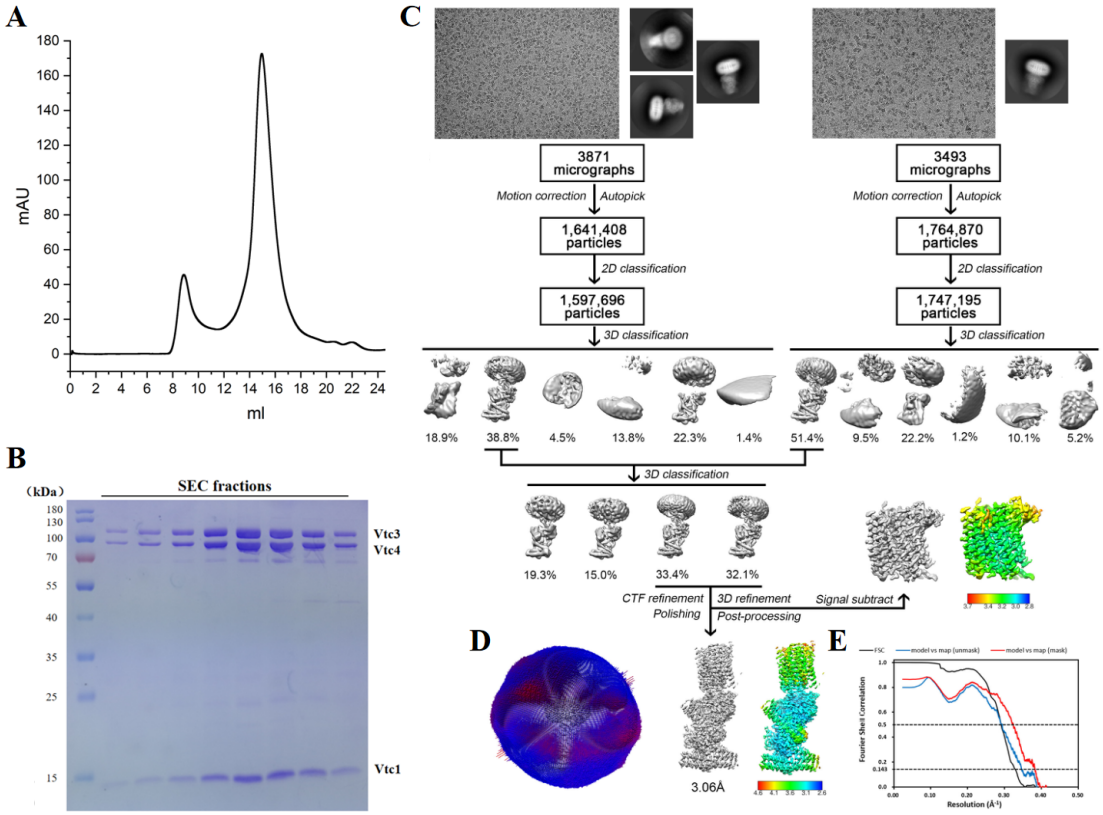

Figure S3. Cryo-EM image processing procedure of the Vtc4/Vtc3/Vtc1 complex.
(A) Size-exclusion chromatography profile of the Vtc4/Vtc3/Vtc1 complex.
(B) The Coomassie blue-stained SDS–PAGE gel of the pooled fractions from A.
(C) Image processing workflow for the Vtc4/Vtc3/Vtc1 complex.
(D) Angular distribution of particles used in the final reconstruction of the 3D map.
(E) Gold-standard Fourier shell correlations of the final 3D reconstruction of the Vtc4/Vtc3/Vtc1 complex, and the validation of the correlation curves of the atomic model by comparing the model with the final map.

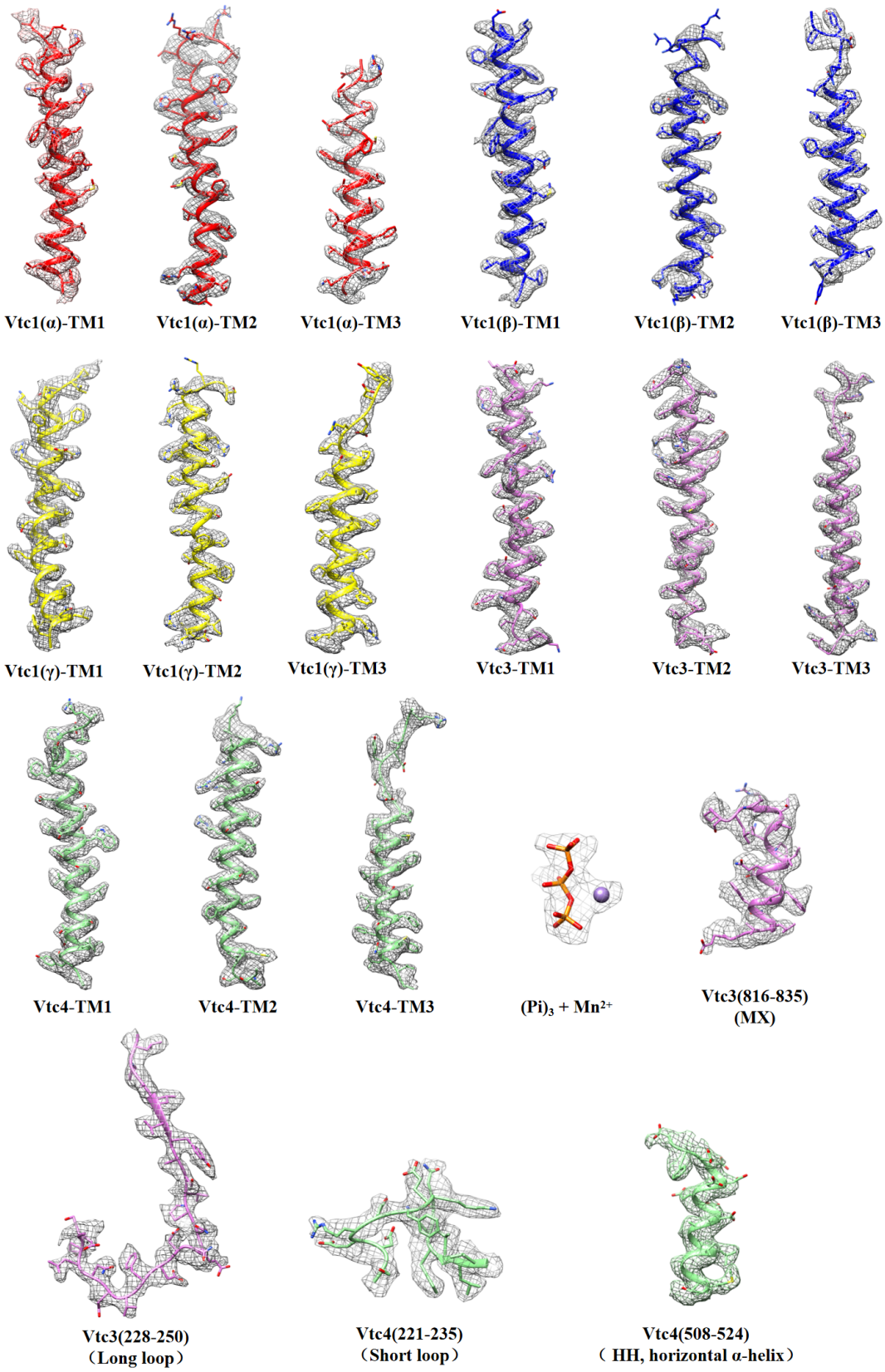

Figure S4. The fitting of the atomic model and the 3D map in selected regions. 3D density maps and atomic models of selected regions in each of the five Vtc4/Vtc3/Vtc1 subunits, as well as the densities of atomic models of the triphosphate

969 and Mn^{2+}. MX, amphiphilic helix; HH, horizontal α-helix. For clarity, Vtc1(α),
970 Vtc1(β) and Vtc1(γ) are colored in red, blue, and yellow, respectively.

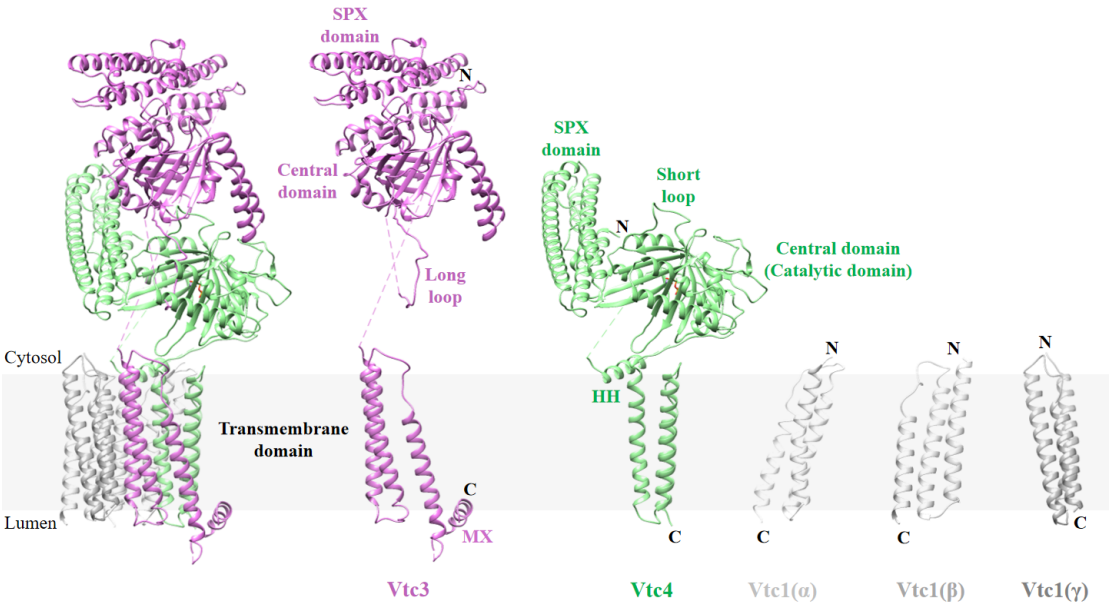

971
972 **Figure S5. The structure of the five Vtc4/Vtc3/Vtc1 subunits.**
973 Structures of the five Vtc4/Vtc3/Vtc1 subunits shown separately. MX, amphipathic
974 helix; HH, horizontal α-helix.
975

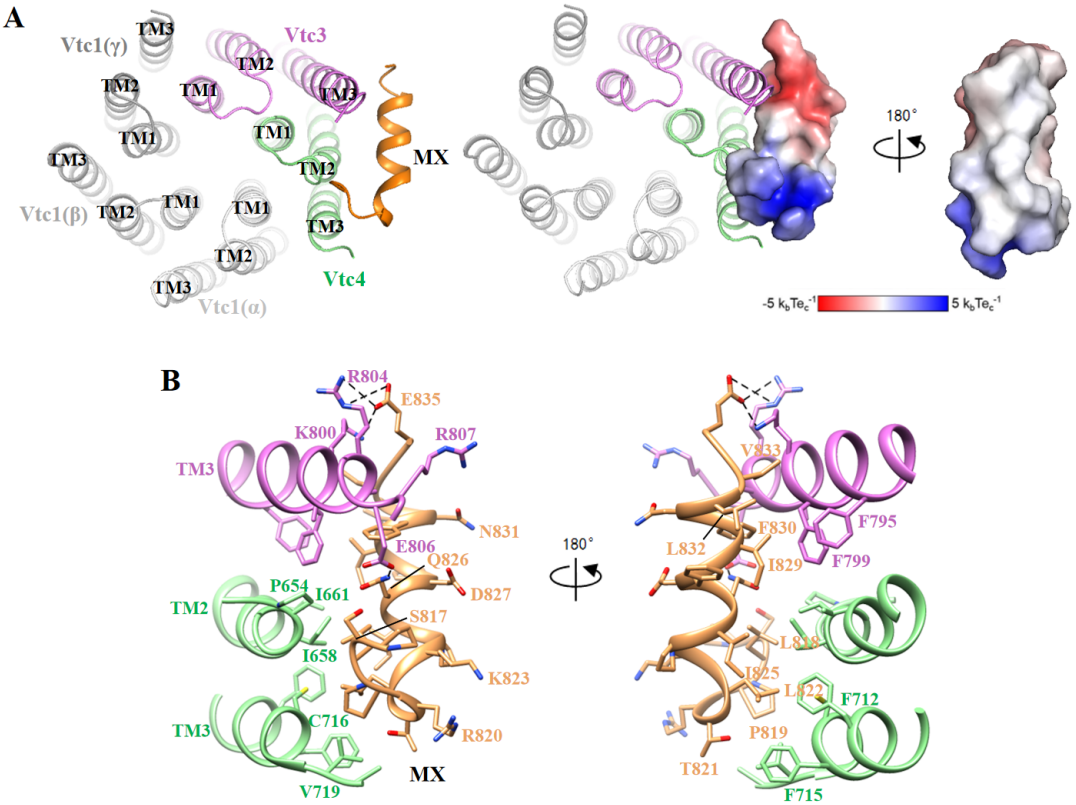

Figure S6. The structure of the MX helix of Vtc3.

(A) Structure and electrostatic surface potential of the MX helix. The side of the MX helix close to the membrane is very hydrophobic, and the side distal from the membrane is very hydrophilic. MX is shown in sandy brown.

(B) The interaction between the MX helix of Vtc3 and the transmembrane domain.

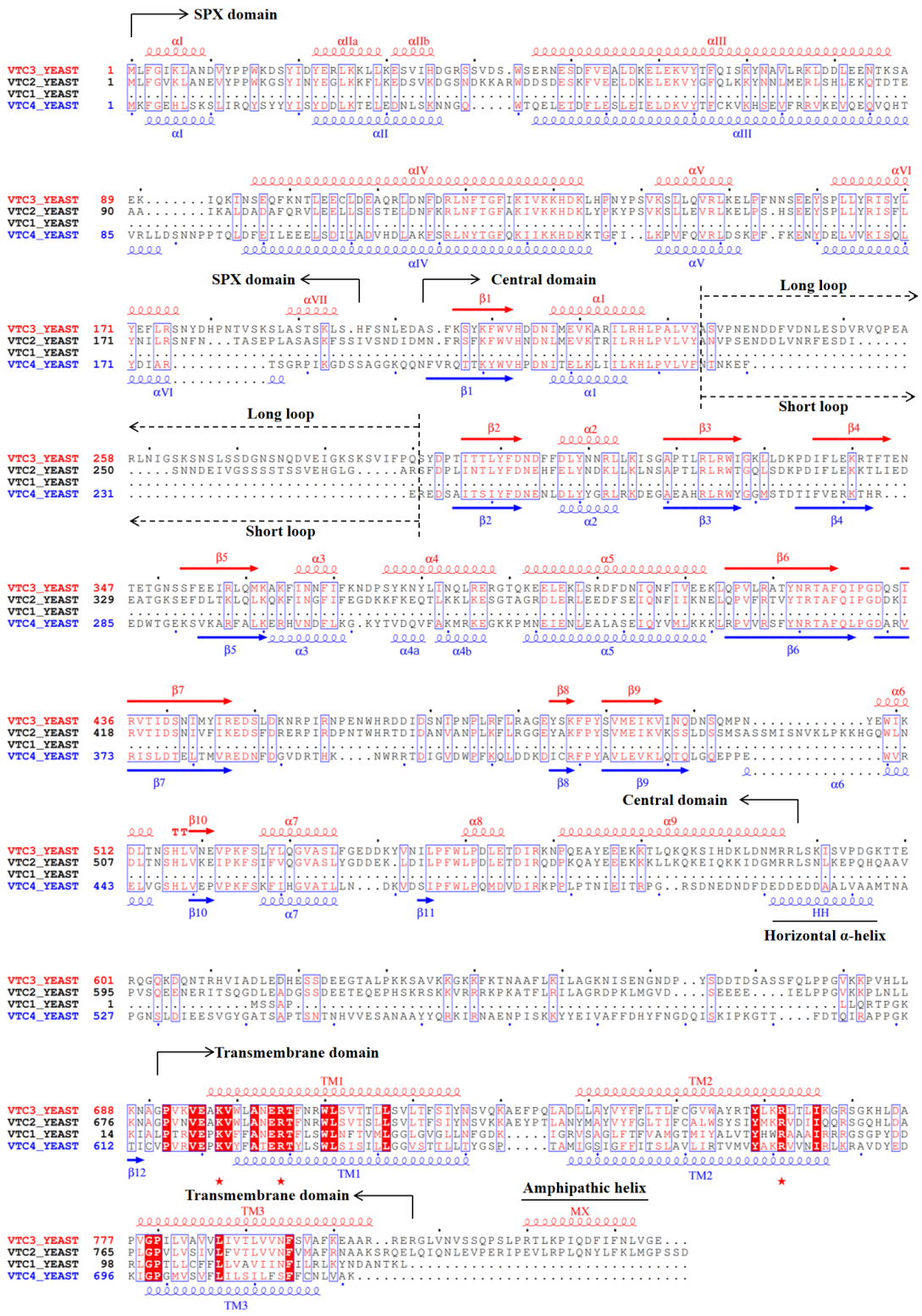

Figure S7. Sequence alignment of Vtc4, Vtc3, Vtc2 and Vtc1.
Helices and β-strands are shown as coils and arrows, respectively. The assignments are produced by ESPript 3.0 (https://espript.ibcp.fr/ESPript/ESPript/) based on the structures S.c. Vtc3 (this study) and S.c. Vtc4 (this study). Key features are marked above the sequences. The red pentagram represents some conserved amino acids.

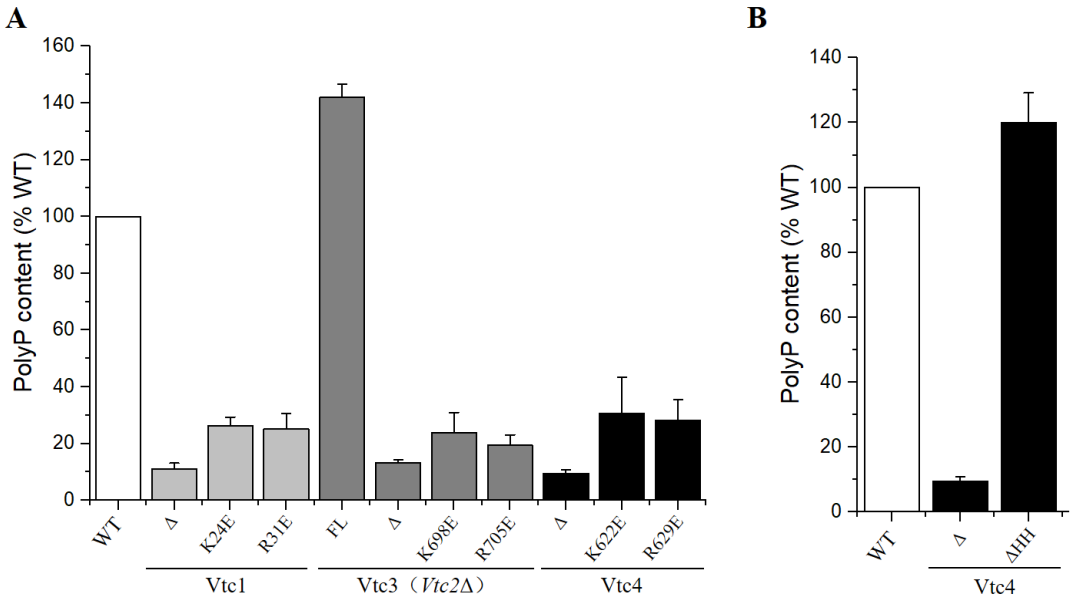

991
992 **Figure S8. Mutational analysis of the polyP channel of the VTC complex.**
993 (A) Cellular polyP content of *VTC4, VTC3* and *VTC1* point mutants expressed under
994 the control of their native promoters in the *vtc4Δ*, *vtc3Δ*(*vtc2Δ*) and *vtc1Δ*
995 backgrounds, respectively. Δ indicates that the entire subunit was knocked out. FL
996 indicates full length, indicating that the subunit has not been modified in any way.
997 Data show the mean±s.d (n=3).
998 (B) Cellular polyP content of *vtc4Δ* cells expressing Vtc4 with truncated horizontal
999 helices under the control of its native promoter. Δ indicates that the entire subunit was
1000 knocked out. Data show the mean±s.d (n=3).
1001
1002

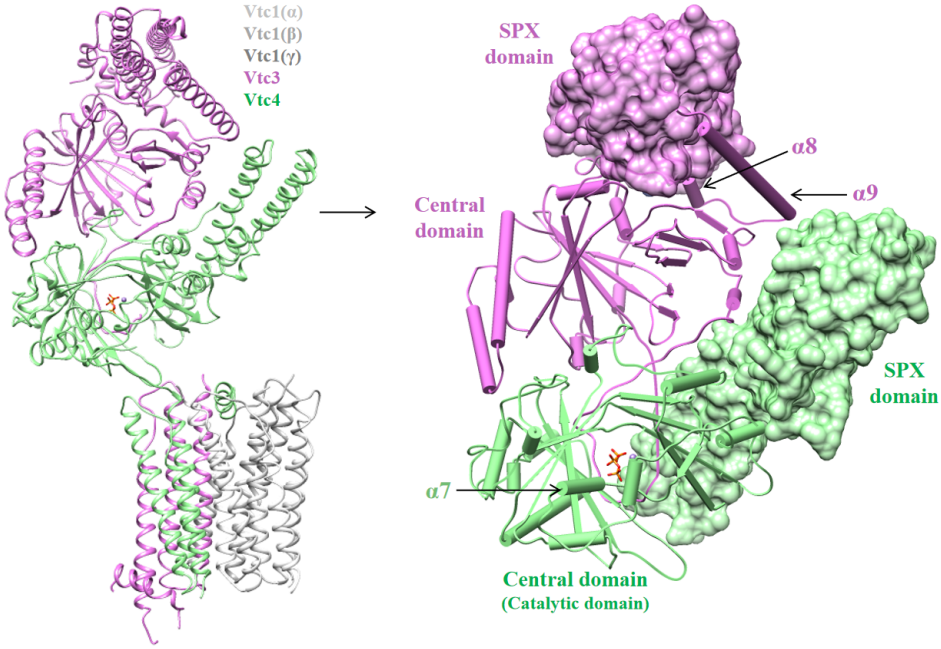

Figure S9. The cytoplasmic domain of Vtc3 and the cytoplasmic domain of Vtc4 form an asymmetric heterodimer.
Both the cytoplasmic domain of Vtc3 and the cytoplasmic domain of Vtc4 contain an SPX domain and a central domain, and the central domain of Vtc3 has no catalytic activity.

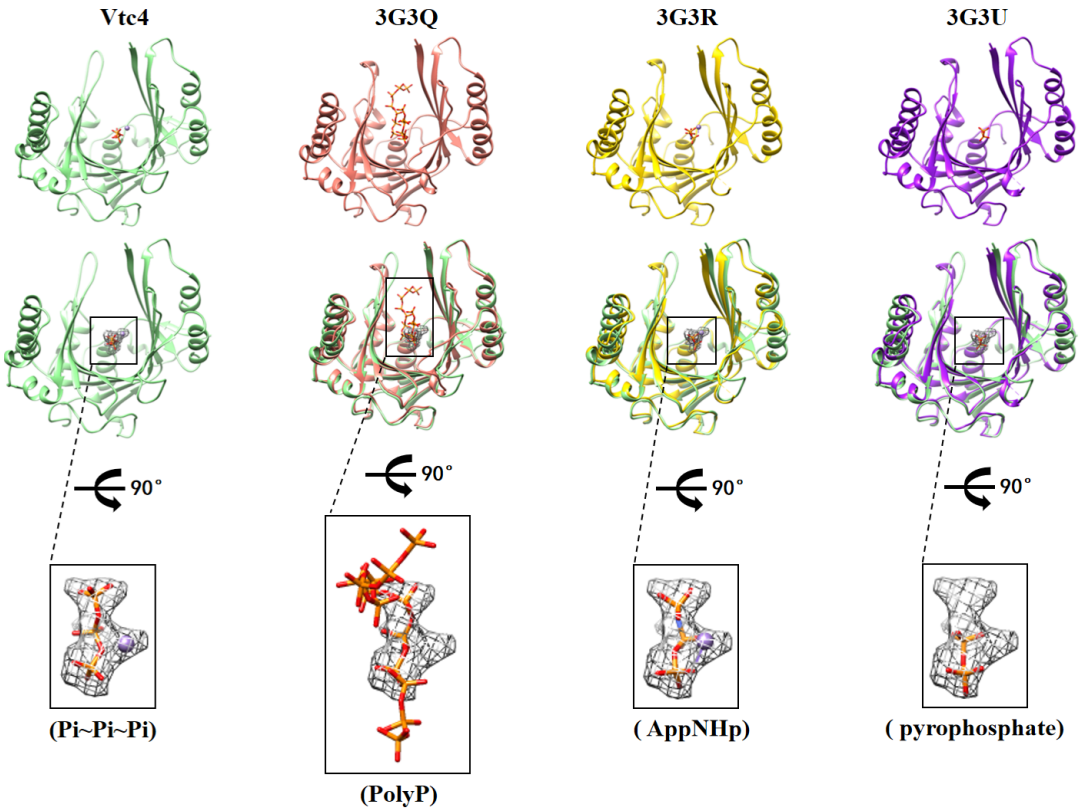

Figure S10. The structures of the central domain of Vtc4 (this study) were compared with those of the polyP-bound Vtc4 central domain (PDB: 3G3Q), the AppNHp-bound Vtc4 central domain (PDB: 3G3R) and the pyrophosphate-bound Vtc4 central domain (PDB: 3G3U), respectively.
The positions of polyP, AppNHp (adenosine-5'-[(β, γ)-imido] triphosphate) and pyrophosphate overlap with the triphosphates in our structure.

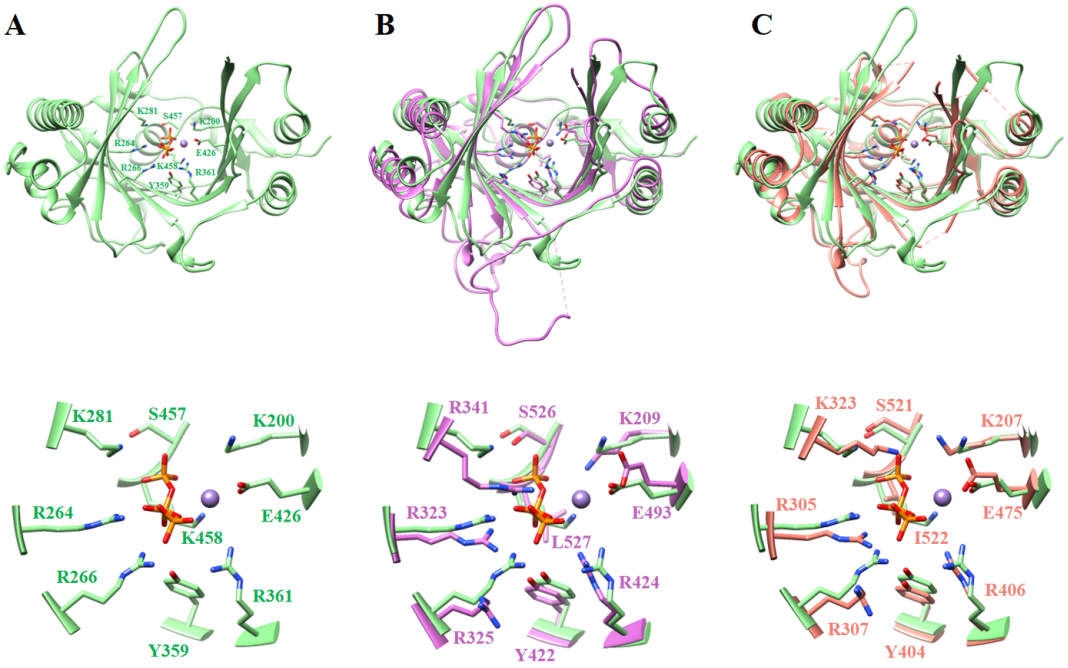

D

Vtc4	K200	R264	R266	K281	Y359	R361	E426	S457	K458
Vtc3	K209	R323	R325	R341	Y422	R424	E493	S526	L527
Vtc2	K207	R305	R307	K323	Y404	R406	E475	S521	I522

Figure S11. Structural comparison of the central domains of Vtc4, Vtc3 and Vtc2.

(A) Structure of the central domain of Vtc4 (from this study). The triphosphate and Mn^{2+} are shown in orange and brown, respectively. Some key residues are shown.

(B) Comparison of the structures of the central domains of Vtc4 and Vtc3. The structures of the central domain of Vtc4 and Vtc3 are from our study. The key amino acids are highly conserved, only K458 of Vtc4 is replaced by L527 of Vtc3.

(C) Comparison of the structures of the central domains of Vtc4 (from this study) and Vtc2 (PDB: 3G3O). The key amino acids are highly conserved, only K458 of Vtc4 is replaced by I522 in Vtc2.

(D) Highly conserved amino acids in the central domain of Vtc4, Vtc3 and Vtc2. Non-conserved amino acids are circled in red boxes.

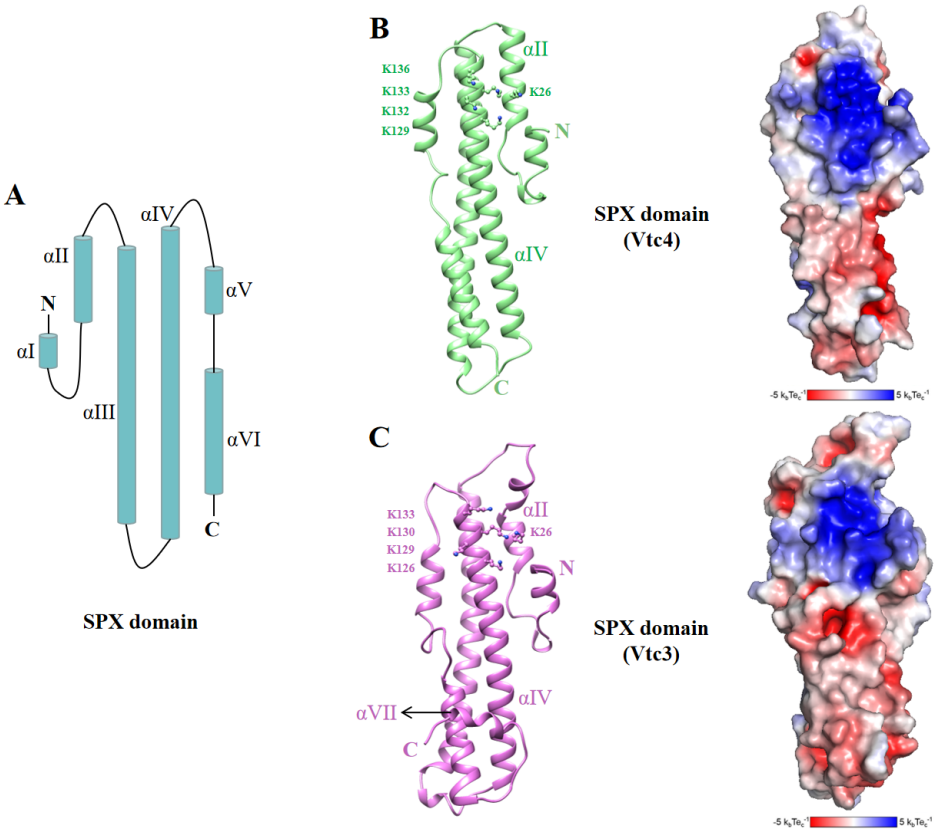

Figure S12. Structures of the SPX domain of Vtc3 and the SPX domain of Vtc4.
(A) Schematic representation of the SPX domain. The SPX domain consists of six α-helices, α I-α VI.
(B) Structure and electrostatic surface potential of the SPX domain of Vtc4, obtained in this study. Key amino acids on the basic surface are highlighted.
(C) Structure and electrostatic surface potential of the SPX domain of Vtc3, obtained in this study. Key amino acids on the basic surface are highlighted.

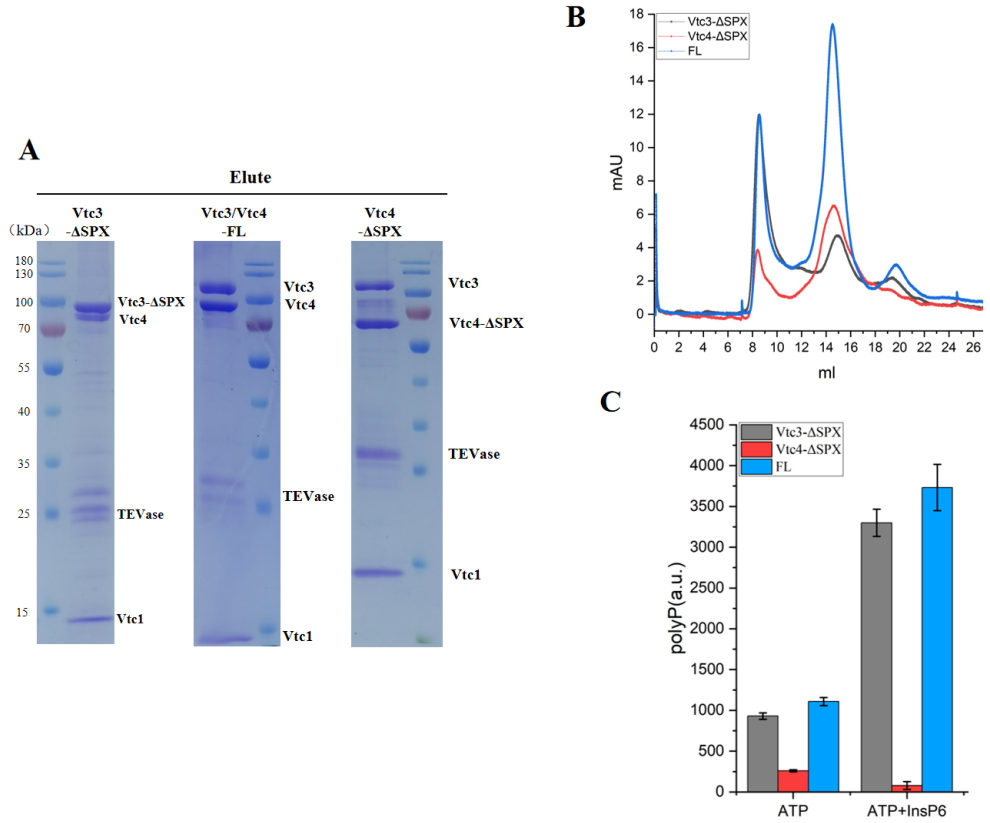

Figure S13. Purification of truncated Vtc4(ΔSPX)/Vtc3/Vtc1 complex and Vtc4/Vtc3(ΔSPX)/Vtc1 complex.

(A) Coomassie blue-stained SDS–PAGE gel of the purified truncated Vtc4(ΔSPX)/Vtc3/Vtc1 complex, Vtc4/Vtc3(ΔSPX)/Vtc1 complex and Vtc4/Vtc3/Vtc1 complex.

(B) Size-exclusion chromatography profile of the truncated Vtc4(ΔSPX)/Vtc3/Vtc1 complex, Vtc4/Vtc3(ΔSPX)/Vtc1 complex and Vtc4/Vtc3/Vtc1 complex.

(C) Purified truncated Vtc4(ΔSPX)/Vtc3/Vtc1 complex, Vtc4/Vtc3(ΔSPX)/Vtc1 complex and Vtc4/Vtc3/Vtc1 complex synthesize polyP in the absence or presence $InsP_6$ *in vitro*. The reaction system is detailed in Methods. Data show the mean±s.d (n=3).

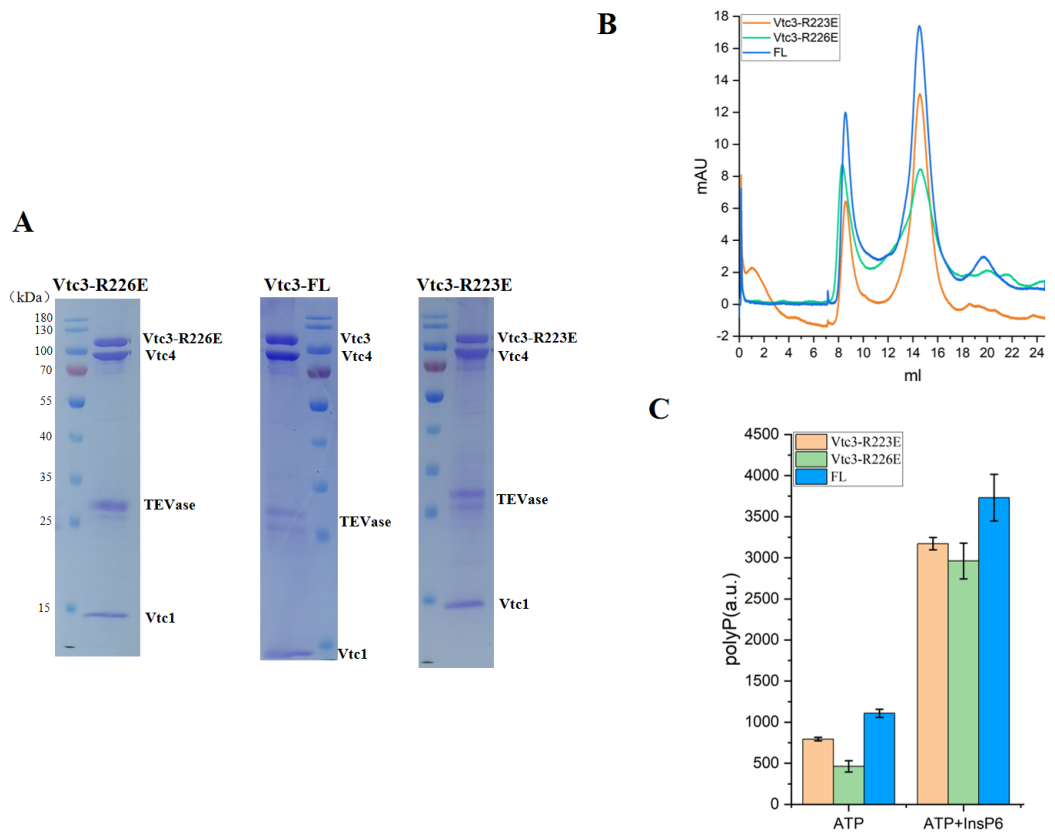

Figure S14. Purification of mutant Vtc4/Vtc3(R223E)/Vtc1 complex and Vtc4/Vtc3(R226E)/Vtc1 complex.

(A) Coomassie blue-stained SDS–PAGE gel of the mutant Vtc4/Vtc3(R223E)/Vtc1 complex, Vtc4/Vtc3(R226E)/Vtc1 complex and Vtc4/Vtc3/Vtc1 complex.

(B) Size-exclusion chromatography profile of the mutant Vtc4/Vtc3(R223E)/Vtc1 complex, Vtc4/Vtc3(R226E)/Vtc1 complex and Vtc4/Vtc3/Vtc1 complex.

(C) Purified mutant Vtc4/Vtc3(R223E)/Vtc1 complex, Vtc4/Vtc3(R226E)/Vtc1 complex and Vtc4/Vtc3/Vtc1 complex synthesize polyP in the absence or presence $InsP_6$ *in vitro*. The reaction system is detailed in Methods. Data show the mean±s.d (n=3).

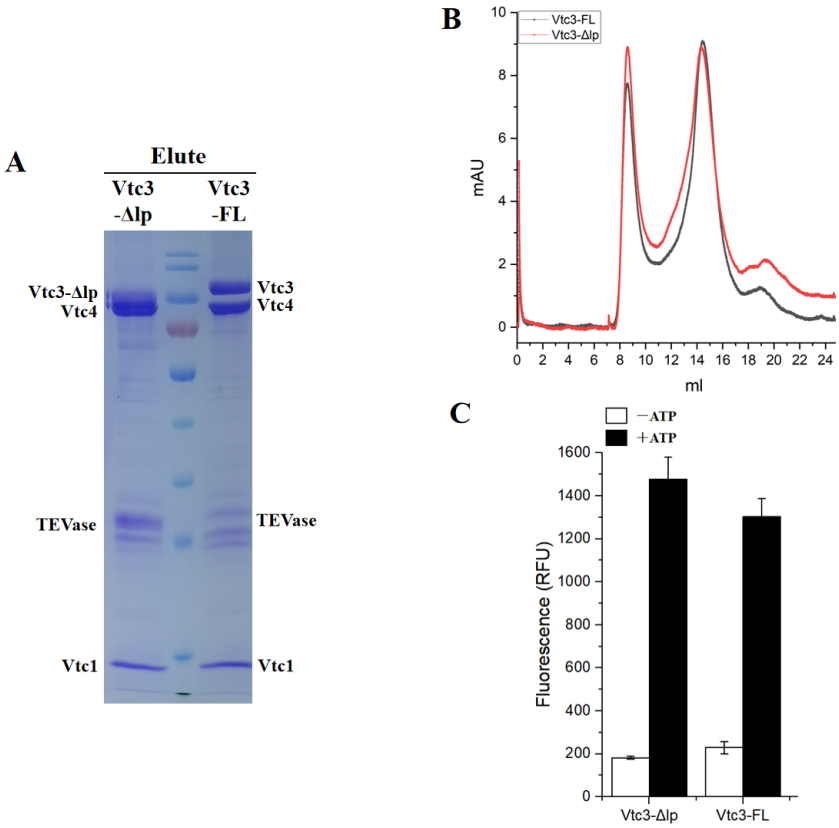

Figure S15. Purification of truncated Vtc4/Vtc3(Δlp)/Vtc1 complexes.
(A) Coomassie blue-stained SDS–PAGE gel of the purified truncated Vtc4/Vtc3(Δlp)/Vtc1 complex and Vtc4/Vtc3/Vtc1 complex. The molecular weights of the marker bands from top to bottom are 180kDa, 130kDa, 100kDa, 70kDa, 55kDa, 40kDa, 35kDa, 25kDa, 15kDa, 10kDa.
(B) Size-exclusion chromatography profiles of the truncated Vtc4/Vtc3(Δlp)/Vtc1 complex and Vtc4/Vtc3/Vtc1 complex.
(C) Purified truncated Vtc4/Vtc3(Δlp)/Vtc1 complexes synthesize polyP in the absence or presence ATP *in vitro*. The reaction system is detailed in Methods. Data show the mean±s.d (n=3).

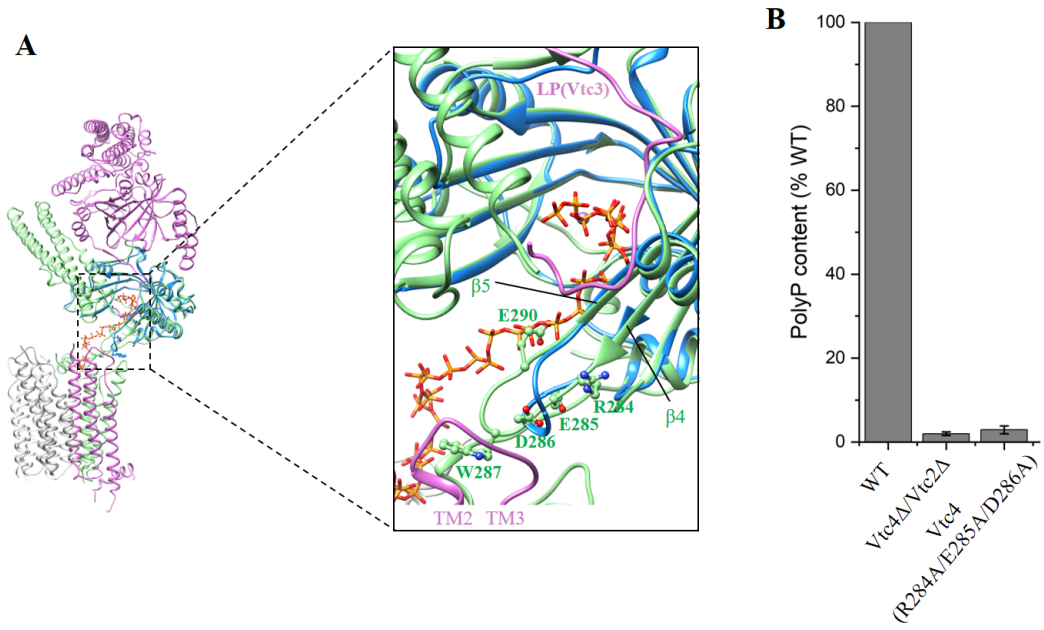

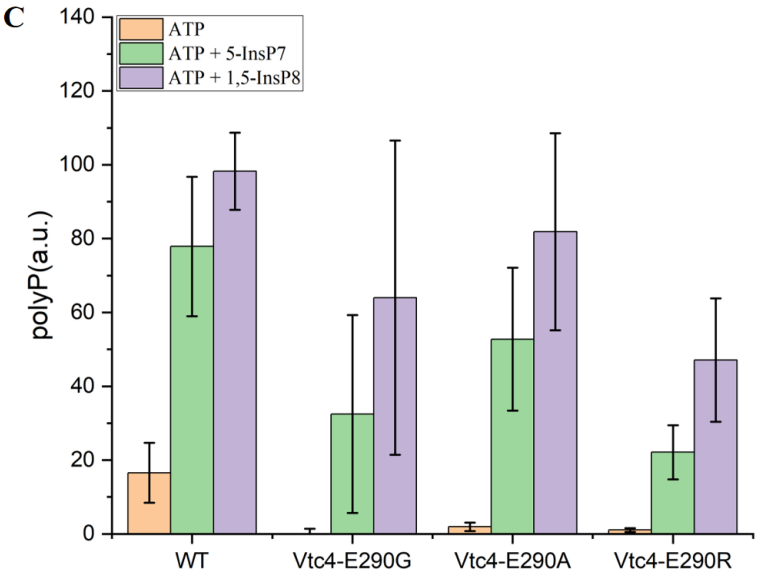

Figure S16. Superposition of the central domain of Vtc4 and the central domain of the polyP-bound Vtc4 (PDB: 3G3Q) structures.

(A) The structure of the central domain of polyP-bound Vtc4 is shown in blue. The polyP chains are shown in orange to overlap the triphosphates.

(B) Cellular polyP content with Vtc4p point mutants expressed under the control of its native promoter in the *vtc4Δ* background. Δ indicates that the entire subunit was knocked out. Data show the mean±s.d (n=3).

(C) PolyP synthesis by isolated vacuoles carrying Vtc4(E290G)/Vtc3/Vtc1 complex, Vtc4(E290A)/Vtc3/Vtc1 complex, Vtc4(E290R)/Vtc3/Vtc1 complex, or Vtc4/Vtc3/Vtc1 complex, assayed in the absence or presence of 1 μM 5-$InsP_7$ or 1,5-$InsP_8$ *in vitro*. The reaction system is detailed in Methods. Data show the mean±s.d (n=3).

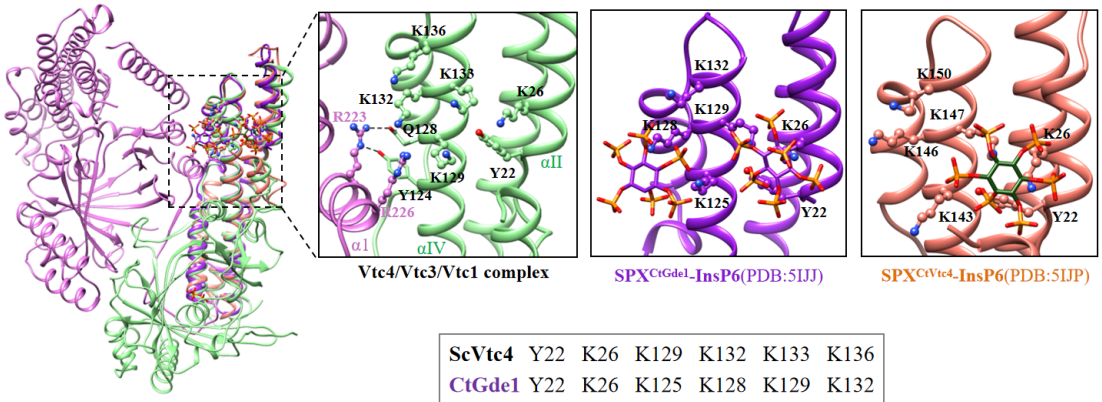

ScVtc4	Y22	K26	K129	K132	K133	K136
CtGde1	Y22	K26	K125	K128	K129	K132
CtVtc4	Y22	K26	K143	K146	K147	K150

Figure S17. Superposition of the structures of SPX^{CtGde1}-$InsP_6$ (PDB: 5IJJ), SPX^{CtVtc4}-$InsP_6$ (PDB: 5IJP) and the SPX domain of Vtc4.
The black box summarizes the conserved lysines that make up the basic InsPP-binding surface.

1099 **Table S1. Cryo-EM data collection, refinement and validation statistics**

	VTC4/3/1 complex (EMDB) (PDB)
Data collection and processing	
Magnification	105,000
Voltage (kV)	300
Electron exposure (e^-/Å^2)	54
Defocus range (μm)	-1.0 ~ -1.5
Pixel size (Å)	0.851
Symmetry imposed	C1
Initial particle projections (no.)	3,406,278
Final particle projections (no.)	1,042,873
Map resolution (Å)	3.06
FSC threshold	0.143
Map resolution range (Å)	2.9-9.8
Refinement	
Initial model used	AlphaFold2
Model resolution (Å)	3.1
FSC threshold	0.5
Map sharpening B factor (Å^2)	-97.4
Model composition	
Non-hydrogen atoms	13,166
Protein residues	1,594
Ligand	6
B-factors (Å^2)	
Protein	0.81/113.97/54.94
Ligand	34.06/93.82/78.03
R.m.s. deviations	
Bond lengths (Å)	0.002
Bond angles (^{o})	0.493
Validation	
MolProbity score	1.27
Clashscore	4.28
Rotamer outliers (%)	0.00
CaBLAM outliers （%）	1.68
Ramachandran plot	
Favored (%)	97.71
Allowed (%)	2.29
Disallowed (%)	0.00

1100
1101

1102 **Table S2. Strains used in this study**

Strain	Relevant genotype	Source
BJ2168	MATa: leu2-3, trp1-289, ura3-52, prb1-1122, pep4-3, prc1-407, gal2	Laboratory
BJ2168 *Vtc1Δ*	VTC1::kanMX	This study
BJ2168 *Vtc2Δ*	VTC2::kanMX	This study
BJ2168 *Vtc3Δ*	VTC3::kanMX	This study
BJ2168 *Vtc2Δ Vtc3Δ*	VTC2::URA3 VTC3::kanMX	This study
BJ2168 *Vtc4Δ*	VTC4::kanMX	This study
BJ2168 Vtc2-TAPm	VTC2-TAPm-kanMX	This study
BJ2168 Vtc3-TAPm	VTC3-TAPm-kanMX	This study
BJ2168 Vtc2-TAPm Vtc3-Strep	VTC2-TAPm-kanMX VTC3-Strep-URA3	This study
BJ2168 Vtc3-TAPm Vtc2-Strep	VTC3-TAPm-kanMX VTC2-Strep-URA3	This study
BJ2168 Vtc3(ΔC24)-TAPm	VTC3(ΔC24)-TAPm-kanMX	This study
BJ2168 Vtc3(ΔC24)-TAPm *Vtc2Δ*	VTC3(ΔC24)-TAPm-kanMX VTC2::URA3	This study
BJ2168 Vtc3(Δlp)-TAPm	VTC3(Δlp)-TAPm-URA3	This study
BJ2168 Vtc3(ΔSPX)-TAPm	VTC3(ΔSPX)-TAPm-URA3	This study
BJ2168 Vtc3-TAPm Vtc4(ΔSPX)	VTC3-TAPm-LEU2 VTC4(ΔSPX)-URA3	This study
BJ2168 Vtc3(R223E)-TAPm	VTC3(R223E)-TAPm-URA3	This study
BJ2168 Vtc3(R226E)-TAPm	VTC3(R226E)-TAPm-URA3	This study
BJ2168 Vtc1(K24E)	VTC1::kanMX VTC1(K24E)-URA3	This study
BJ2168 Vtc1(E30A)	VTC1::kanMX VTC1(E30A)-URA3	This study
BJ2168 Vtc1(E30R)	VTC1::kanMX VTC1(E30R)-URA3	This study
BJ2168 Vtc1(R31E)	VTC1::kanMX VTC1(R31E)-URA3	This study
BJ2168 Vtc1(R83A)	VTC1::kanMX VTC1(R83A)-URA3	This study
BJ2168 Vtc1(R83E)	VTC1::kanMX VTC1(R83E)-URA3	This study
BJ2168 Vtc3(K698E) *Vtc2*Δ	VTC3::kanMX VTC3(K698E)-LEU2 VTC2::URA3	This study
BJ2168 Vtc3(V699D) *Vtc2*Δ	VTC3::kanMX VTC3(V699D)-LEU2 VTC2::URA3	This study
BJ2168 Vtc3(E704A) *Vtc2*Δ	VTC3::kanMX VTC3(E704A)-LEU2 VTC2::URA3	This study
BJ2168 Vtc3(E704R) *Vtc2*Δ	VTC3::kanMX VTC3(E704R)-LEU2 VTC2::URA3	This study
BJ2168 Vtc1(R705E) *Vtc2*Δ	VTC3::kanMX VTC3(R705E)-LEU2 VTC2::URA3	This study
BJ2168 Vtc3(R762A) *Vtc2*Δ	VTC3::kanMX VTC3(R762A)-LEU2 VTC2::URA3	This study
BJ2168 Vtc3(R762E) *Vtc2*Δ	VTC3::kanMX VTC3(R762E)-LEU2 VTC2::URA3	This study
BJ2168 Vtc3(L765D) *Vtc2*Δ	VTC3::kanMX VTC3(L765D)-LEU2 VTC2::URA3	This study
BJ2168 Vtc3(L774D) *Vtc2*Δ	VTC3::kanMX VTC3(L774D)-LEU2 VTC2::URA3	This study
BJ2168 Vtc4(ΔHH)	VTC4::kanMX VTC4(ΔHH)-URA3	This study
BJ2168 Vtc4(R196E)	VTC4::kanMX VTC4(R196E)-URA3	This study
BJ2168 Vtc4(K200A)	VTC4::kanMX VTC4(K200A)-URA3	This study
BJ2168 Vtc4(R253E)	VTC4::kanMX VTC4(R253E)-URA3	This study
BJ2168 Vtc4(K256E)	VTC4::kanMX VTC4(R256E)-URA3	This study
BJ2168 Vtc4(R264A)	VTC4::kanMX VTC4(R264A)-URA3	This study
BJ2168 Vtc4(R266A)	VTC4::kanMX VTC4(R266A)-URA3	This study
BJ2168 Vtc4(R264A/R266A)	VTC4::kanMX VTC4(R264A/R266A)-URA3	This study
BJ2168 Vtc4(K281A)	VTC4::kanMX VTC4(K281A)-URA3	This study

BJ2168 Vtc4(W287D）	VTC4::kanMX VTC4(W287D)-URA3	This study
BJ2168 Vtc4(K291E)	VTC4::kanMX VTC4(K291E)-URA3	This study
BJ2168 Vtc4(K294E)	VTC4::kanMX VTC4(K294E)-URA3	This study
BJ2168 Vtc4(Y359F)	VTC4::kanMX VTC4(Y359F)-URA3	This study
BJ2168 Vtc4(R361A)	VTC4::kanMX VTC4(R361A)-URA3	This study
BJ2168 Vtc4(R373E)	VTC4::kanMX VTC4(R373E)-URA3	This study
BJ2168 Vtc4(E426A)	VTC4::kanMX VTC4(E426A)-URA3	This study
BJ2168 Vtc4(K428E)	VTC4::kanMX VTC4(K428E)-URA3	This study
BJ2168 Vtc4(K455E)	VTC4::kanMX VTC4(K455E)-URA3	This study
BJ2168 Vtc4(S457A）	VTC4::kanMX VTC4(S457A)-URA3	This study
BJ2168 Vtc4(K458L）	VTC4::kanMX VTC4(K458L)-URA3	This study
BJ2168 Vtc4(K458I）	VTC4::kanMX VTC4(K458I)-URA3	This study
BJ2168 Vtc4(K458A）	VTC4::kanMX VTC4(K458A)-URA3	This study
BJ2168 Vtc4(R618E)	VTC4::kanMX VTC4(R618E)-URA3	This study
BJ2168 Vtc4(P621D）	VTC4::kanMX VTC4(P621D)-URA3	This study
BJ2168 Vtc4(K622E)	VTC4::kanMX VTC4(K622E)-URA3	This study
BJ2168 Vtc4(E628A)	VTC4::kanMX VTC4(E628A)-URA3	This study
BJ2168 Vtc4(E628R)	VTC4::kanMX VTC4(E628R)-URA3	This study
BJ2168 Vtc4(R629E)	VTC4::kanMX VTC4(R629E)-URA3	This study
BJ2168 Vtc4(R681A)	VTC4::kanMX VTC4(R681A)-URA3	This study
BJ2168 Vtc4(R681E)	VTC4::kanMX VTC4(R681E)-URA3	This study

TAPm is a modified TAP tag consisting of 6His-TEV-Protein A.

1105 **Table S3. Oligonucleotides used in this study**

Oligonucleotides	Sequence
Vtc2-TAPm-F	5'-CCACTTCAAAATTATCTATTCAAGTTAATGGGGCCAAGCAGTGATCGTACGCTGCAGGTCGAC-3'
Vtc2-TAPm-R	5'-ACATTACAAACATAAAAACACATGGTCTCAGTAGATAGAGTACATATCGATGAATTCGAGCTCG-3'
Vtc3-TAPm-F	5'-ACACTAAAACCAATTCAAGATTTTATCTTCAATTTGGTTGGGGAACGTACGCTGCAGGTCGAC-3'
Vtc3-TAPm-R	5'-CTGGTACTTGTGTAATATATGTGTATATAAAAAATATACATGTTCATCGATGAATTCGAGCTCG-3'
Vtc2-Strep-F	5'-CCACTTCAAAATTATCTATTCAAGTTAATGGGGCCAAGCAGTGATAAGCTTTGGAGCCACCCCCAG-3'
Vtc2-Strep-R	5'-ACATTACAAACATAAAAACACATGGTCTCAGTAGATAGAGTACATACTGAGAGTGCACCATACCAC-3'
Vtc3-Strep-F	5'-ACACTAAAACCAATTCAAGATTTTATCTTCAATTTGGTTGGGGAAAAGCTTTGGAGCCACCCCCAG-3'
Vtc3-Strep-R	5'-CTGGTACTTGTGTAATATATGTGTATATAAAAAATATACATGTTCACTGAGAGTGCACCATACCAC-3'
Vtc1Δ-F	5'-CTACATTATCGAATACGATTAAACACTACGCCAGATTTCCACAATTCACCCGGCCAGCGACATG-3'
Vtc1Δ-R	5'-TACAGTTTGTGCGTAACCCACGCTTACGATATTGGAATTACAATTATCGATGAATTCGAGCTCG-3'
Vtc2Δ-F	5'-AGTAGAAAGAACGACTACACCTCAACATAACGACACTTTTTTGACTCACCCGGCCAGCGACATG-3'
Vtc2Δ-R	5'-TTACAAACATAAAAACACATGGTCTCAGTAGATAGAGTACATATTATCGATGAATTCGAGCTCG-3'
Vtc3Δ-F	5'-TTAGAGCGAACAGCAGAATTTGTCCTTGGTTTTCAGAGTTTGAAATCACCCGGCCAGCGACATG-3'
Vtc3Δ-R	5'-CTGGTACTTGTGTAATATATGTGTATATAAAAAATATACATGTTCATCGATGAATTCGAGCTCG-3'
Vtc4Δ-F	5'-CAATCAAATCGGCCAATAAAAGAGCATAACAAGGCAGGAACAGCTTCACCCGGCCAGCGACATG-3'
Vtc4Δ-R	5'-TATGATTATTACTTAATTATACAGTAAAAAAAACACGCTGTGTATATCGATGAATTCGAGCTCG-3'

1106

1107 **References:**

1108 Adams PD, Afonine PV, Bunkoczi G, Chen VB, Davis IW, Echols N, Headd JJ, Hung LW, Kapral GJ,
1109 Grosse-Kunstleve RW *et al* (2010) PHENIX: a comprehensive Python-based system for macromolecular
1110 structure solution. *Acta Crystallogr D Biol Crystallogr* 66: 213-221
1111 Akiyama M, Crooke E, Kornberg A (1992) The polyphosphate kinase gene of Escherichia coli. Isolation
1112 and sequence of the ppk gene and membrane location of the protein. *J Biol Chem* 267: 22556-22561

1113 Ansermet C, Moor MB, Centeno G, Auberson M, Hu DZ, Baron R, Nikolaeva S, Haenzi B, Katanaeva N,
1114 Gautschi I *et al* (2017) Renal Fanconi Syndrome and Hypophosphatemic Rickets in the Absence of
1115 Xenotropic and Polytropic Retroviral Receptor in the Nephron. *J Am Soc Nephrol* 28: 1073-1078
1116 Austin S, Mayer A (2020) Phosphate Homeostasis - A Vital Metabolic Equilibrium Maintained Through
1117 the INPHORS Signaling Pathway. *Front Microbiol* 11: 1367
1118 Azevedo C, Livermore T, Saiardi A (2015) Protein polyphosphorylation of lysine residues by inorganic
1119 polyphosphate. *Mol Cell* 58: 71-82
1120 Azevedo C, Singh J, Steck N, Hofer A, Ruiz FA, Singh T, Jessen HJ, Saiardi A (2018) Screening a Protein
1121 Array with Synthetic Biotinylated Inorganic Polyphosphate To Define the Human PolyP-ome. *Acs*
1122 *Chemical Biology* 13: 1958-1963
1123 Bentley-DeSousa A, Holinier C, Moteshareie H, Tseng YC, Kajjo S, Nwosu C, Amodeo GF, Bondy-
1124 Chorney E, Sai Y, Rudner A *et al* (2018) A Screen for Candidate Targets of Lysine Polyphosphorylation
1125 Uncovers a Conserved Network Implicated in Ribosome Biogenesis. *Cell Rep* 22: 3427-3439
1126 Bondy-Chorney E, Abramchuk I, Nasser R, Holinier C, Denoncourt A, Baijal K, McCarthy L, Khacho M,
1127 Lavallee-Adam M, Downey M (2020) A Broad Response to Intracellular Long-Chain Polyphosphate in
1128 Human Cells. *Cell Rep* 33
1129 Bru S, Jimenez J, Canadell D, Arino J, Clotet J (2016a) Improvement of biochemical methods of polyP
1130 quantification. *Microb Cell* 4: 6-15
1131 Bru S, Martinez-Lainez JM, Hernandez-Ortega S, Quandt E, Torres-Torronteras J, Marti R, Canadell D,
1132 Arino J, Sharma S, Jimenez J *et al* (2016b) Polyphosphate is involved in cell cycle progression and
1133 genomic stability in Saccharomyces cerevisiae. *Mol Microbiol* 101: 367-380
1134 Cohen A, Perzov N, Nelson H, Nelson N (1999) A novel family of yeast chaperons involved in the
1135 distribution of V-ATPase and other membrane proteins. *J Biol Chem* 274: 26885-26893
1136 Desfougeres Y, Gerasimaite RU, Jessen HJ, Mayer A (2016) Vtc5, a Novel Subunit of the Vacuolar
1137 Transporter Chaperone Complex, Regulates Polyphosphate Synthesis and Phosphate Homeostasis in
1138 Yeast. *J Biol Chem* 291: 22262-22275
1139 Docampo R, Huang G (2016) Acidocalcisomes of eukaryotes. *Curr Opin Cell Biol* 41: 66-72
1140 Emsley P, Cowtan K (2004) Coot: model-building tools for molecular graphics. *Acta Crystallogr D Biol*
1141 *Crystallogr* 60: 2126-2132
1142 Funakoshi M, Hochstrasser M (2009) Small epitope-linker modules for PCR-based C-terminal tagging
1143 in Saccharomyces cerevisiae. *Yeast* 26: 185-192
1144 Gerasimaite R, Mayer A (2016) Enzymes of yeast polyphosphate metabolism: structure, enzymology
1145 and biological roles. *Biochem Soc Trans* 44: 234-239
1146 Gerasimaite R, Pavlovic I, Capolicchio S, Hofer A, Schmidt A, Jessen HJ, Mayer A (2017) Inositol
1147 Pyrophosphate Specificity of the SPX-Dependent Polyphosphate Polymerase VTC. *ACS Chem Biol* 12:
1148 648-653
1149 Gerasimaite R, Sharma S, Desfougeres Y, Schmidt A, Mayer A (2014) Coupled synthesis and
1150 translocation restrains polyphosphate to acidocalcisome-like vacuoles and prevents its toxicity. *J Cell*
1151 *Sci* 127: 5093-5104
1152 Gray MJ, Wholey WY, Wagner NO, Cremers CM, Mueller-Schickert A, Hock NT, Krieger AG, Smith EM,
1153 Bender RA, Bardwell JCA *et al* (2014) Polyphosphate Is a Primordial Chaperone. *Molecular Cell* 53:
1154 689-699

Hassanian SM, Dinarvand P, Smith SA, Rezaie AR (2015) Inorganic polyphosphate elicits pro-inflammatory responses through activation of the mammalian target of rapamycin complexes 1 and 2 in vascular endothelial cells. *J Thromb Haemost* 13: 860-871

Hoac B, Kiffer-Moreira T, Millan JL, McKee MD (2013) Polyphosphates inhibit extracellular matrix mineralization in MC3T3-E1 osteoblast cultures. *Bone* 53: 478-486

Holmstrom KM, Marina N, Baev AY, Wood NW, Gourine AV, Abramov AY (2013) Signalling properties of inorganic polyphosphate in the mammalian brain. *Nature Communications* 4

Hothorn M, Neumann H, Lenherr ED, Wehner M, Rybin V, Hassa PO, Uttenweiler A, Reinhardt M, Schmidt A, Seiler J *et al* (2009) Catalytic core of a membrane-associated eukaryotic polyphosphate polymerase. *Science* 324: 513-516

Ikeh M, Ahmed Y, Quinn J (2017) Phosphate Acquisition and Virulence in Human Fungal Pathogens. *Microorganisms* 5

Ingram SW, Barnes LD (2000) Disruption and overexpression of the Schizosaccharomyces pombe aph1 gene and the effects on intracellular diadenosine 5 ',5 "'-P-1,P-4-tetraphosphate (Ap(4)A), ATP and ADP concentrations. *Biochemical Journal* 350: 663-669

Jumper J, Evans R, Pritzel A, Green T, Figurnov M, Ronneberger O, Tunyasuvunakool K, Bates R, Zidek A, Potapenko A *et al* (2021) Highly accurate protein structure prediction with AlphaFold. *Nature*

Klompmaker SH, Kohl K, Fasel N, Mayer A (2017) Magnesium uptake by connecting fluid-phase endocytosis to an intracellular inorganic cation filter. *Nature Communications* 8

Lander N, Ulrich PN, Docampo R (2013) Trypanosoma brucei Vacuolar Transporter Chaperone 4 (TbVtc4) Is an Acidocalcisome Polyphosphate Kinase Required for in Vivo Infection. *Journal of Biological Chemistry* 288: 34205-34216

Legati A, Giovannini D, Nicolas G, Lopez-Sanchez U, Quintans B, Oliveira JRM, Sears RL, Ramos EM, Spiteri E, Sobrido MJ *et al* (2015) Mutations in XPR1 cause primary familial brain calcification associated with altered phosphate export. *Nature Genetics* 47: 579-581

Liu J, Yang L, Luan M, Wang Y, Zhang C, Zhang B, Shi J, Zhao FG, Lan W, Luan S (2015) A vacuolar phosphate transporter essential for phosphate homeostasis in Arabidopsis. *Proc Natl Acad Sci U S A* 112: E6571-6578

Lonetti A, Szijgyarto Z, Bosch D, Loss O, Azevedo C, Saiardi A (2011) Identification of an evolutionarily conserved family of inorganic polyphosphate endopolyphosphatases. *J Biol Chem* 286: 31966-31974

Mailer RK, Hanel L, Allende M, Renne T (2019) Polyphosphate as a Target for Interference With Inflammation and Thrombosis. *Front Med-Lausanne* 6

McCarthy L, Abramchuk I, Wafy G, Denoncourt A, Lavallee-Adam M, Downey M (2022) Ddp1 Cooperates with Ppx1 to Counter a Stress Response Initiated by Nonvacuolar Polyphosphate. *Mbio* 13

Moreno-Sanchez D, Hernandez-Ruiz L, Ruiz FA, Docampo R (2012) Polyphosphate Is a Novel Pro-inflammatory Regulator of Mast Cells and Is Located in Acidocalcisomes. *Journal of Biological Chemistry* 287: 28435-28444

Muller O, Bayer MJ, Peters C, Andersen JS, Mann M, Mayer A (2002) The Vtc proteins in vacuole fusion: coupling NSF activity to V(0) trans-complex formation. *EMBO J* 21: 259-269

Nair VS, Gu CF, Janoshazi AK, Jessen HJ, Wang HC, Shears SB (2018) Inositol pyrophosphate synthesis by diphosphoinositol pentakisphosphate kinase-1 is regulated by phosphatidylinositol (4,5) bisphosphate. *Bioscience Rep* 38

Ozalp VC, Nielsen LJ, Olsen LF (2010) An Aptamer-Based Nanobiosensor for Real-Time Measurements of ATP Dynamics. *Chembiochem* 11: 2538-2541

Pettersen EF, Goddard TD, Huang CC, Couch GS, Greenblatt DM, Meng EC, Ferrin TE (2004) UCSF Chimera--a visualization system for exploratory research and analysis. *J Comput Chem* 25: 1605-1612

Pluskal T, Hayashi T, Saitoh S, Fujisawa A, Yanagida M (2011) Specific biomarkers for stochastic division patterns and starvation-induced quiescence under limited glucose levels in fission yeast. *Febs J* 278: 1299-1315

Puga MI, Mateos I, Charukesi R, Wang Z, Franco-Zorrilla JM, de Lorenzo L, Irigoyen ML, Masiero S, Bustos R, Rodriguez J *et al* (2014) SPX1 is a phosphate-dependent inhibitor of Phosphate Starvation Response 1 in Arabidopsis. *Proc Natl Acad Sci U S A* 111: 14947-14952

Rohloff P, Docampo R (2008) A contractile vacuole complex is involved in osmoregulation in Trypanosoma cruzi. *Exp Parasitol* 118: 17-24

Schepler H, Neufurth M, Wang SF, She ZD, Schroder HC, Wang XH, Muller WEG (2022) Acceleration of chronic wound healing by bio-inorganic polyphosphate: In vitro studies and first clinical applications. *Theranostics* 12: 18-34

Sethuraman A, Rao NN, Kornberg A (2001) The endopolyphosphatase gene: essential in Saccharomyces cerevisiae. *Proc Natl Acad Sci U S A* 98: 8542-8547

Smith SA, Morrissey JH (2014) Polyphosphate: a new player in the field of hemostasis. *Curr Opin Hematol* 21: 388-394

Voglmaier SM, Bembenek ME, Kaplin AI, Dormán G, Olszewski JD, Prestwich GD, Snyder SH (1996) Purified inositol hexakisphosphate kinase is an ATP synthase: diphosphoinositol pentakisphosphate as a high-energy phosphate donor. *Proceedings of the National Academy of Sciences* 93: 4305-4310

Wild R, Gerasimaite R, Jung JY, Truffault V, Pavlovic I, Schmidt A, Saiardi A, Jessen HJ, Poirier Y, Hothorn M *et al* (2016) Control of eukaryotic phosphate homeostasis by inositol polyphosphate sensor domains. *Science* 352: 986-990

Williams CJ, Headd JJ, Moriarty NW, Prisant MG, Videau LL, Deis LN, Verma V, Keedy DA, Hintze BJ, Chen VB *et al* (2018) MolProbity: More and better reference data for improved all-atom structure validation. *Protein Sci* 27: 293-315

Zhang K (2016) Gctf: Real-time CTF determination and correction. *J Struct Biol* 193: 1-12

Zheng SQ, Palovcak E, Armache JP, Verba KA, Cheng Y, Agard DA (2017) MotionCor2: anisotropic correction of beam-induced motion for improved cryo-electron microscopy. *Nat Methods* 14: 331-332

Zivanov J, Nakane T, Scheres SHW (2020) Estimation of high-order aberrations and anisotropic magnification from cryo-EM data sets in RELION-3.1. *Iucrj* 7: 253-267